AN ABSTRACT OF THE THESIS OF

Stebby Varghese John for the degree of Master of Science in Chemical Engineering presented on November 20, 2018.

Title: Device Fabrication and Characterization for Biological and Radiation Sensing

Abstract approved:

_____

Gregory S. Herman

Amorphous indium gallium zinc oxide (IGZO) thin film transistors (TFT) has revolutionized the display industry enabling smaller pixel sizes and higher refreshing rates than traditional amorphous Si: H TFTs. These attributes of IGZO were leveraged to make a field-effect sensing (FES) platform capable of sensing various biomarkers. The sensitivity and selectivity of the sensor to glucose was achieved by functionalizing the IGZO back channel surface with aminosilane groups which were further cross-linked with glucose oxidase (GO_x) enzymes. The sensor was integrated with a microfluidic channel, and the sensor response was studied with respect to varying glucose concentrations. An analysis of the sensitivity of the sensor for various gate voltages (V_G) was conducted to determine the optimal V_G to operate the sensor for continuous glucose sensing. These sensing platforms can be made completely transparent and are compatible for integration onto flexible substrates enabling transparent active-matrix sensing arrays (TASA) where multiple biomarkers can be sensed which will aid next-generation internet of things (IoT) hardware for human health monitoring and analytics.

Lead selenide (PbSe) nanocrystalline (NC) particles have a large Bohr radius (~ 46 nm) which enables high quantum confinement effects in relatively larger diameter NC PbSe. As a

consequence, the efficiency of charge multiplication (CM) on impact ionization (II) is enhanced for NC compared to bulk PbSe. In addition, a relatively high density of these NC PbSe enables complete transfer of high energy radiation in a relatively thin sensing layer. However, the radiation sensing capability and electronic transport for NC PbSe radiation detectors is impeded by long-chain stabilizing organic ligands on the NC surface as well as the current fabrication methods. In this research, a biphasic ligand exchange process was integrated to the detector fabrication protocol to improve electrical conductivity by reducing interparticle distance and improved packing efficiency. In addition, the fabrication complexity of the radiation sensors was greatly reduced due to solution based ligand exchange, which can be scalable in achieving thick, crack free NC PbSe films. Improved conductivity and Schottky like behavior, which are desirable for good radiation sensing, were demonstrated in the fabricated NC PbSe radiation detector.

Device Fabrication and Characterization for Biological and Radiation Sensing

by
Stebby Varghese John

A THESIS

submitted to

Oregon State University

in partial fulfillment of
the requirements for the
degree of

Master of Science

Presented November 20, 2018
Commencement June 2019

Master of Science thesis of Stebby Varghese John presented on November 20, 2018

APPROVED:

Major Professor, representing Chemical Engineering

Head of the School of Chemical, Biological, and Environmental Engineering

Dean of the Graduate School

I understand that my thesis will become part of the permanent collection of Oregon State University libraries. My signature below authorizes release of my thesis to any reader upon request.

Stebby Varghese John, Author

ACKNOWLEDGEMENTS

I would like to mention my deepest gratitude to Dr. Gregory S. Herman for providing me an opportunity to do research in his group. His patience, support, and guidance throughout were critical for completion of this work. I'm indebted to him for the technical knowledge and professional values he has instilled in me through our conversations and through his own example. I extend my gratitude to Dr. Haori Yang from Nuclear Engineering for his support and technical guidance.

Also, I would like to thank the graduate students from Dr. Herman's research group for their support and counsel throughout the research. I would like to acknowledge Mr. Joe Bergevin for his involvement and support during my research. I would like to thank Dr. Matt Graham at Physics department for providing access to his UV Vis NIR spectrophotometer for this research. I also acknowledge the support from the CBEE staff during my time here at Oregon State University.

I thank my Dad and Mom for their unconditional love, support, and prayers. Their insightful and inspiring words have always been my forte.

Above all, I thank God for this life, his provisions and countless blessings.

TABLE OF CONTENTS

TABLE OF CONTENTS (Continued)

Page

LIST OF FIGURES

Figure Page

LIST OF FIGURES (continued)

Figure Page

LIST OF FIGURES (continued)

Figure Page

LIST OF FIGURES (continued)

Figure Page

LIST OF TABLES

Table Page

Chapter 1: Introduction

Sensors

Sensors have become ubiquitous in our daily lives and play a crucial component towards improving the quality of life [1]. Over the past few years, efforts to integrate sensors into the surroundings has led to miniaturization, improved efficacy, and reduced power consumption [2]. Application and development of transparent semiconducting materials like indium tin oxide (ITO) and indium gallium zinc oxide (IGZO) along with advances in flexible electronic technologies has opened possibilities for invisible sensors that integrate well into the ecosystem [3][4]. The advent of semiconducting nanocrystalline materials and the ability to tune their properties with size and composition enable us to develop and envisage electronics that enable applications in chemical sensing, nuclear radiation detection and biomolecule identification [5]. The concept of predictive analytics and treatment in personalized medicine, and internet of things (IoT) has augmented the demand for wearable sensors in recent years [4]. The new generation of wearable sensors has the potential to deliver real-time, fast and continuous measurement of relevant information, opening avenues for collecting large sets of data, for example, about human health dynamics which would enable early detection of systemic diseases and personalized treatment regimens [4] [6]. This new paradigm in healthcare was dormant for years, due to the lack of technology to manufacture sensors in a form factor that does not interfere with the mobility of the user. The advancement of flexible electronic technologies with respect to efficient materials and manufacturing has enabled sensors that are wearable and are capable of extracting minimally invasive molecular information through readily accessible bodily fluids like blood, sweat, saliva and tears. Flexible electronics provide a platform for wearable sensors due to its lightweight, low cost, high degree of flexibility and

conformability [7]. The application of nanotechnology in material science, and development of flexible electronics technologies have led to remarkably rapid developments in the field of wearable chemical, biochemical, and radiation sensors, particularly during the past few years [4].

Biosensors

A biosensor is a device comprising two elements: (i) bioreceptor and (ii) transducer. These biosensors are capable of complex analyte detection. Modeled after the biological systems, the bioreceptors creates an interactive interface with the analyte of interest. These interactions are quantified by the transducers by measuring signals that are proportional to the analyte concentration in the electrolyte. The signals generated by the transducer are typically electrical (current or voltage), triggered through electrical, optical or thermal impetus as a result of the analyte interaction with the bioreceptor. A variety of immobilization techniques have been developed to attach a gamut of bioreceptors like nucleic acids, antibodies, enzymes, lectins, cell organelles, tissues and microorganisms on various transducer element surfaces [8]. In addition to the bioreceptor and the transducer element, a biosensor encompasses complex electronic circuitry to process the transduced signals, transmit the information, analyze the data and condition it for display. This complex circuitry performs the function of signal amplification and conversion of analog to digital signals. The display is the user interface, in most cases a liquid crystal display (LCD) integrated with a computer that generates easily deducible outputs in the form of numeric, graphics, tabular or an image customized for different end users [9]. Schematic representation of a biosensor is shown in Fig 1.

Application for biosensors in disease detection, environment monitoring, biomarker monitoring, and food safety are aimed at improving the quality of life. To realize these commercial

applications, key attributes like selectivity, sensitivity, reproducibility, stability, and linearity need to be optimized for a biosensor.

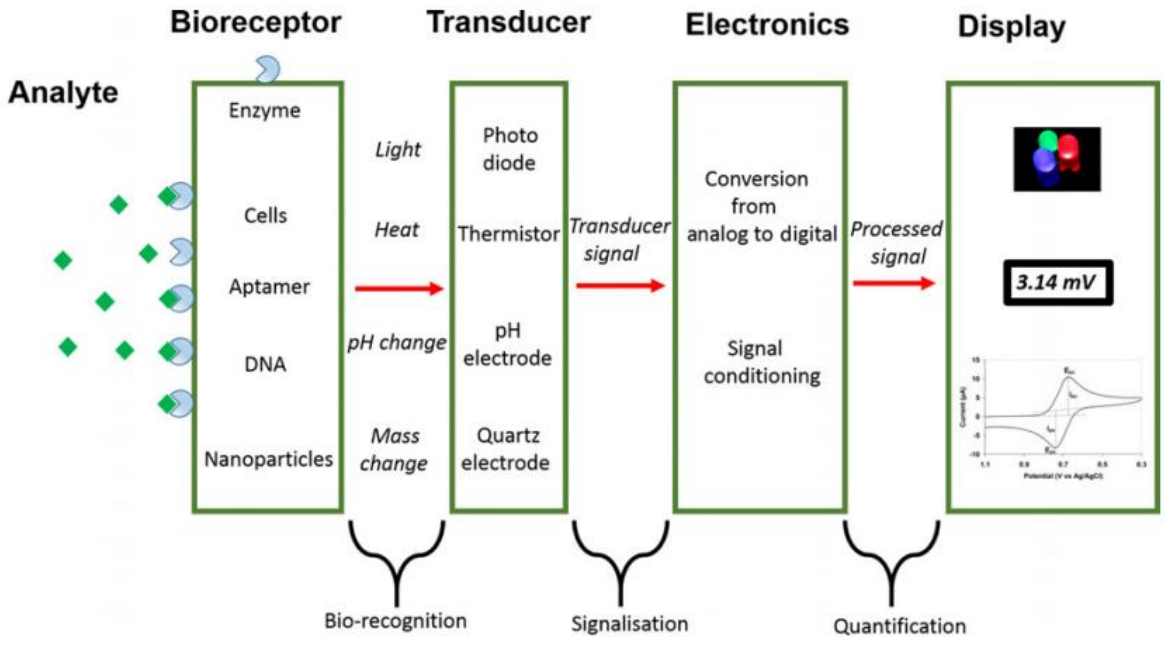

Fig 1. Schematics of a biosensor. Reprinted with permission from (N. F. and P. E. Nikhil Bhalla, Pawan Jolly, "Introduction to Biosensors," *Essays Biochem.*, vol. 60, pp. 1–8, 2016). Copyright 2016 Portland Press.

New materials for transducers and usage of antibodies as bioreceptors have been reported to improve the selectivity and sensitivity for analytes. Du et al. demonstrated excellent selectivity using IGZO field effect transistor (FET) based glucose sensors [3]. These sensors could selectively detect glucose while avoiding interference from acetaminophen and ascorbic acid. This was due to the specific catalytic reaction between glucose oxidase (GO_X) and glucose. [3]. For amperometric glucose sensors, Du et al. reported the ability to minimize or completely eliminate the acetaminophen interference by using permaselective layers of perfluorosulfonic acid (PFSA) for an amperometric glucose sensor fabricated on flexible substrate [10]. Use of novel materials like IGZO, zinc oxide nanorods, graphene/silver nanowires has been reported with high sensitivity

to the analytes of interest [11][3][12]. Good stability, reproducibility, and linearity in response for an acceptable range of analyte concentrations have been reported in devices using these materials as transducers. The miniaturization of biosensors has been proven to be beneficial in many aspects, especially with respect to improving the signal to noise ratio [13]. In nanoscale transducers, the surface to volume ratio of the active sensing area increases. Thus the dimension of the transducer and the target biomarker become comparable, thereby eliminating non-specific binding and enhances the selectivity and sensitivity [9].

In recent years, graphene based nanomaterials has gained interest in the biosensing realm [14]. Graphene is a zero-gap semiconductor, with good conductivity and transparency. In addition graphene is low cost and has low environmental impact, which have promoted its use in many modes of biosensing like in electrical, electrochemical and optical transductions [14]. Integration of graphene, graphene oxide, and carbon nanotubes along with nanowires [12] have transcended the conventional biosensing capabilities. Single-walled carbon nanotubes and modified carbon nanofibers have improved the detection of molecules at the single-cell and subcellular levels achieving detection limits as low as 7.7 nM in case of neurotransmitters like dopamine and epinephrine [15] [16]. Real-time detection of single-stranded DNA with a detection limit of 10 nM with a linear response upto 500 nM was achieved by using gold nanoparticle modified graphene FET sensors [14].

Another class of nanomaterials that are extensively studied for biological and medical applications are quantum dots (QD) [17] . QD's owing to their high photoluminescence quantum yield, narrowband emission peak with broad excitation wavelength, photostability, high luminescence lifetime and high surface to volume ratio has been utilized in applications such as

immunofluorescence assays, cell and animal biology, and DNA array technology [18]. Carrier multiplication (CM) effect in QD nanomaterials makes these fluorophores brighter than conventional commercially available organic dyes. In addition, the photobleaching resistance of QD, ranging from minutes to hours, have made it possible to get well contrasted, crisp images making these nanomaterials ideal for biolabelling applications [18]. A QD based portable fluorescence biosensor for protein biomarkers was developed at Pacific Northwest National Laboratory (PNNL) [19]. This sensor allows rapid and ultrasensitive responses to nitrated ceruloplasmin down to 1 nM. In a diagnostic standpoint, the accurate measurement of these copper carrying proteins in the bloodstream is relevant as lower levels may indicate several issues including Wilson disease, aceruloplasminemia, Menkes disease, and copper deficiency [19]. MicroRNA (miRNA) is a potential biomarker for early detection of cancer. Deng et al. have reported using QD labels to enhance the detection efficiency of the strip-based biosensor that relies on target-recycled non-enzymatic amplification strategy for miRNA quantification [17]. The reported range of detection for these biosensors was between 2–200 fmol with a limit of 200 amol [17]. Recently, novel biosensor platforms have used graphene QDs for miRNA detection [20]. These biosensor platforms with QD enabled technologies for fast, reliable and accurate detection of biomarkers are promising for next generation point of care diagnostics for early cancer detection and other systemic disease diagnostics.

Based on the application and sensing mechanism, a biosensor uses a range of transduction techniques including, electric, electrochemical, optical, piezoelectric, gravimetric, pyroelectric, and acoustic- sensitive approaches. Development of micro and nanofabrication techniques and other paper or strip-based flow techniques have greatly complimented the development of biosensors[4] [19]. Current technologies allow us to fabricate sensors with a desired form factor

and allows targeted delivery of the samples leading to reduced sample requirements. For example, integration of sensors on flexible substrates enables us to measure relevant analytes using contact lens-based sensor or tattoo-based sensors using minute quantity of sample (tear fluid, sweat, etc) [4].

In spite of the extensive research conducted in the biosensing field, commercialization of the lab-based biosensors has seen little success except for glucose sensing and pregnancy testing. A gamut of factors that deter the commercialization efforts may include poor market insight for a specific analyte of interest, lack of clear-cut advantages over existing sensing technology for the analyte detection, lack of packing and storage technology for long-term device stability, higher cost of manufacturing and stringent regulations. However, the gaps are being leveled and the barriers for commercialization are being removed at a fast pace due to strong interdisciplinary research conducted in the biosensing field, bringing people and techniques across fields together to find optimum solutions for the problems faced [9].

Field Effect Sensors

Among various transduction techniques, field effect transistor (FET) based sensing have garnered much attention due to its potential to offer ultra-high sensitivity, low power operations, and cost reduction. The seamless integration potential of FETs with current electronic manufacturing techniques may promote the portability and miniaturization of chemical and biosensors. FETs also hold potential with respect to building active sensing arrays which can provide accurate and parallel sensing capabilities of various analytes through multiplexing. Since the demonstration of FET as an ion selective sensor for pH measurements in the 1970s, a variety of FET architectures and sensing mechanisms, have been incorporated for various analyte sensing [21].

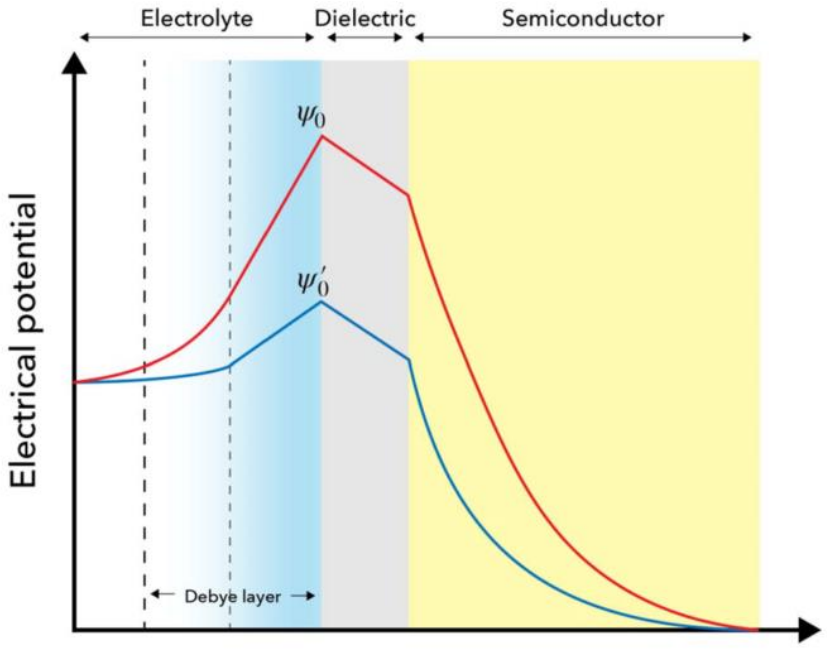

Fig 2. Schematics of a generalized biochemical field effect sensor mechanism. Reprinted with permission from (Y.-C. Syu, W.-E. Hsu, and C.-T. Lin, "Review—Field-Effect Transistor Biosensing: Devices and Clinical Applications," *ECS J. Solid State Sci. Technol.*, vol. 7, no. 7, pp. Q3196–Q3207, 2018).Copyright 2018 Electrochemical Society.

Conventional ion selective membrane is comprised of a metal oxide field effect transistor (MOSFET) with the metal gate replaced by an electrolyte resulting in an oxide – electrolyte interface. This architecture was used to develop the first field effect pH sensor. For a MOSFET, when the metal gate potential is changed, the electric field induces band bending resulting in channel carrier concentration changes. That is when a potential greater than the threshold voltage is applied on the gate, the transistor turns on. Similarly, for a field effect sensor (FES) under this architecture, the gate (electrolyte) potential is governed by factors like the solution potential or the charge of the biomolecule. These factors change the charge carrier concentration in the channel making the threshold voltage shift in the positive or negative direction. The difference in threshold voltage (ΔV_{th}), effects the change in drain current (ΔI_D) which is the measure of sensitivity. The change in potential of the electrolyte ($\Delta\Psi_0 = \Psi_0 - \Psi_0^{'}$) due to intrinsic charge or from ions released

due to biocatalytic reactions at the surface changes the capacitance at the interface (Fig 2). Thus for an ion selective field effect transistor (ISFET) based sensors under discussion, the sensing happens at the electrolyte – dielectric interface. Different architectures of ISFET have been used to improve the sensitivity including extended gate, dual-gate and floating gate ISFETs [22].

In this research, another class of FET called the thin film transistor (TFT) has been used to make FES. From here on our discussions will be based on the TFT based sensors. Under this classification, a number of FESs have been developed for chemical and biological sensing. Silicon nanowire, graphene, zinc oxide, indium tin oxide, and indium gallium zinc oxide are some of the reported materials used as a semiconducting channel in TFT based FES. Contrary to the ISFET, sensing of the analyte happens at the interface between the channel and the electrolyte for TFT based FES. In the ensuing section, the construction, characteristics and operation principle of TFT based FESs are discussed.

Thin Film Transistor

A TFT is a classification of the field effect transistor comprising of 3 terminals viz. source, drain, and gate. The body consists of the source and drain, a semiconductor active channel, gate dielectric, and a gate. A typical TFT in the bottom gated structure is shown in Fig 3.

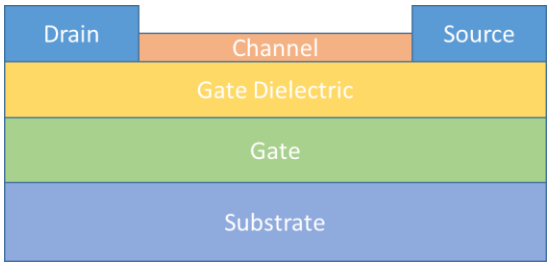

Fig 3. Bottom gated TFT structure

In a TFT, the channel material can be a p-type or n-type semiconductor material based on the relative number of donors and acceptors in a semiconductor. All semiconductors contain acceptor and donor charge states above 0 K. The negatively charged donor states contribute electrons to the conduction band and the positively charged acceptor states contribute holes that can be excited into the valence band. Majority charge carriers in n-type semiconductors are negatively charged electrons, and the majority charge carriers in p-type semiconductors are positively charged holes [23].

Fig 4 shows the band bending in a metal - insulator - semiconductor (MIS) device with an n-type semiconductor under different bias condition. When at equilibrium ($V_D = 0$) the energy bands are flat since the Fermi level of the metal and semiconductor align with each other. However, when a negative bias is applied, the energy bands bend upward at semiconductor – insulator interface and the electrons are pushed away resulting a non-conducting depletion region [24]. When a positive gate potential ($V_G > 0$) is applied, the positive charges at the metal side of the metal-oxide capacitor induce a corresponding negative charge at the semiconductor side. As the positive bias at the gate is increased, the negative charge induced in the semiconductor at the semiconductor - gate dielectric interface increases until the region above the dielectric effectively become an n-type semiconductor region, and current (I_D) can flow between drain and source through the channel formed near the interface. In other words, drain current flow is enabled by the gate potential. Thus in a TFT, the drain current flow can be modulated by the gate voltage; i.e. the transistor can be switched on or off based on the V_G applied. When V_G is greater than the threshold voltage (V_{th}) the device is said to be in an on state and the device is said to be in an off state when $V_{th} > V_G$. This discussion is based on an n-type channel assumption.

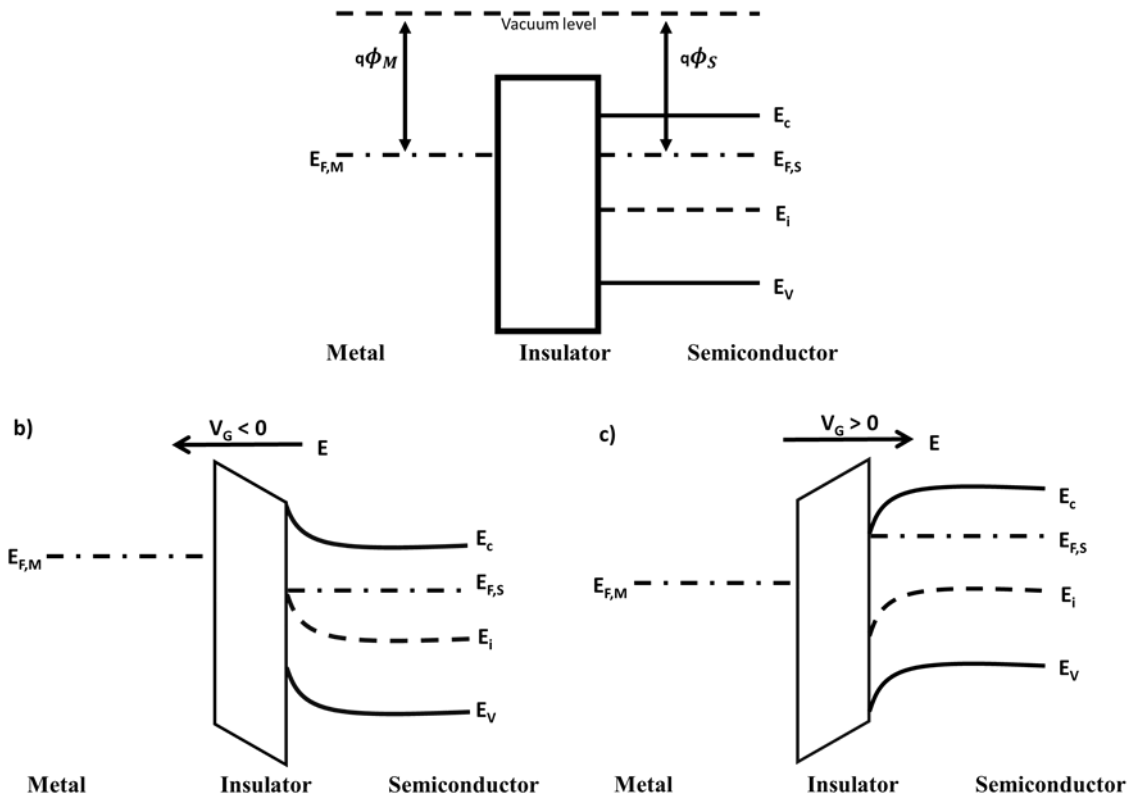

Fig 4. Energy band diagrams depicting the three regimes of operation for MIS structure in n-type TFTs: (a) Equilibrium ($V_G = 0$), (b) Depletion ($V_G < 0$), and (c) Accumulation ($V_G > 0$).

The performance of a TFT is characterized based on several parameters like threshold voltage (V_{th}), field effect mobility (μ_{FE}), subthreshold swing (SS) and the current on to off ratio. The V_{th} is defined as the minimum gate voltage required to generate a conductive pathway within the channel. The μ_{FE} represents the ease with which the majority charge carrier moves in the channel under an electric field. The SS measured in V/decade relates the current output to the gate potential. The I_{on}/I_{off} ratio is the ratio of the drain current in the ON state to the current in the OFF state of the TFT [23]. The extraction and importance of these parameters are explained in detail in chapter 2. IGZO FES are discussed in detail in chapter 3 and its application as a biomarker sensing platform is demonstrated using glucose sensing.

Nuclear Radiation Sensors

Radiation is the emission or transmission of energy in form of waves or particle. Depending on the energy of the particles, radiation can be broadly classified into ionizing and non - ionizing radiation. Radiation with energy greater than 10 eV are ionizing radiation since they can ionize atoms and molecules, and break chemical bonds. Nuclear radiation generated as a result of nuclear decay process or nuclear reactions, such as alpha particles, beta particles, gamma rays, and neutrons fall under this category. X-rays emitted from an excited atom is also ionizing radiation. A wide spectrum of lower frequency electromagnetic waves including ultraviolet, visible light, infrared, microwaves, radio waves and thermal waves are considered as non-ionizing.

Ionizing radiation can cause damage to living tissues and cells. Exposure to ionizing radiation may cause skin burn, internal organ failure, hair loss or death. Prolonged exposure may increase the chance of cancer in living organisms or even catalyze genetic mutation. However, controlled exposure to ionizing radiation has applications in cancer treatment, medical imaging, and material characterization techniques such as x-ray photoelectron spectroscopy (XPS), x-ray diffraction (XRD), small angle x-ray spectroscopy (SAXS), and x-ray absorption spectroscopy (XAS) to name a few. Radiation detectors are an integral part of the nuclear facility instrumentation. Facilities like nuclear power plants or synchrotrons need radiation detectors to measure radiation levels and to ensure safe operation. As nuclear technology is fast evolving with new types of fast breeder reactors, neutron source facilities using fast and cold neutrons, and accelerator-based facilities, the need for improvement in the current radiation detection technology is warranted to allow precise detection with high resolution.

Existing detector technology can be classified based on the medium used for sensing: a) gas-filled detectors, b) single crystal and liquid scintillators, and c) semiconductor materials. The measurement of ionizing radiation is based on the non-equilibrium charge states induced when the radiation interacts with the above-mentioned medium. The ion-electron or electron-hole pair generated during this event is sensed by the electric field induced due to the device architecture or the photons generated due to the radiative recombination of the electron-hole pairs are detected using a scintillation photon detector [25]. Gas-filled detectors take advantage of large multiplication of ion pairs when incident by ionizing radiation. The ions thus generated are accelerated towards the charged electrodes creating a measurable current. Reduced pressures and high voltage are used to promote the inelastic collisions, increase the mean free path of the electron, and to reduce recombination losses [26]. When every ion is collected, with minimum losses due to recombination, the maximum current is obtained (i.e., saturation current which will be proportional to the intensity of radiation). Typically, gas-filled detectors have air as a medium which requires 35 eV to produce charge carriers [26][27]. The scintillation detectors depend on the fact that suitable "flours" give off pulses of light when traversed by a charged particle [26]. The scintillations produced by the fluors are electromagnetic radiations in visible or ultraviolet region generated due to the excitation and de-excitation of the electrons in the fluor. This light is directed on to a photomultiplier cathode where it ejects electrons by the photo-electric effect to generate an electric pulse proportional to the radiation intensity. Sodium iodide is a widely used inorganic scintillation material [26]. In a semiconductor radiation detector, incident radiation generates electron-hole pairs, which are collected at the electrodes to generate an electrical impulse. These pulses contain information on the type, energy, and a number of particles per unit time. The common semiconductor materials used in these detectors are Si and Ge. Si-based radiation detectors can produce detection when incident radiation has an energy of

3.66 eV. Similarly, high purity germanium (HPGe) with a band gap of 0.7 eV requires 2.80 eV energy to excite electron-hole pairs [28] [29]. When compared to the gas medium detectors, the average energy required to produce an electron-hole pair is an order of magnitude less than for semiconductor-based detectors. This results in more accurate measurements are possible with excellent energy resolution. However, these detectors are expensive and bulky in form factor (HPGe detectors requires liquid N_2 cooling for room temperature operation) making this technology unsuitable for ubiquitous next-generation radiation detectors.

Nanostructured Materials for Radiation Sensing

Two distinct approaches using nanostructured media for radiation sensing have being studied in recent years: Nano scintillators (NS) and nanocrystal (NC) assemblies as a semiconductor device. The motivation behind using nanostructured materials is that the phonon-assisted loss processes can be minimized compared to single-crystal materials, leading to higher conversion efficiency of the incident radiation into information carriers (charge, phonon) that participate in signal formation [30].

Nano scintillators

Nano scintillators are nanocrystalline material that scintillates on incident radiation. As mentioned above, the interest of the radiation detection community in incorporating NS materials stems from the fact that when in comparison to single crystalline materials, nanostructured scintillators exhibit more rapid and enhanced light emission due to the suppression of non-radiative loss processes, which yields in theory, higher imaging performance for radiation detection [25].

CdSe/ZnS nano scintillators impregnated on a nanoporous glass composite has been reported to exhibit a two-factor increase in energy resolution compared to conventional NaI detectors [31]. Rare earth doped fluorides and oxide materials like CaF_2: Eu, BaF_2: Ce, LaF_3: Eu, and $LuBO_3$ has also been reported by various research groups to have radiation enabled scintillation [30]. Recent work by Liu et al. demonstrated γ ray scintillating detectors using CdZnS/ZnS QD in transparent polymer nanocomposite with 9.8% energy resolution [32]. The schematic representation of the scintillation process and the different routes of fluorescence resonance energy transfer (FRET) in this nano-scintillating device is shown in Fig 5. However, severe transmittance loss in bulk NC due to QD aggregation still poses the biggest hurdle against their application as scintillators [32].

Semiconducting Nanocrystals

Strong quantum confinement in NC particles leads to generation of multiexcitons from a single incident photon (impact ionization). Quick and efficient extraction of these charge carriers generated through impact ionization can be utilized in making radiation detectors [30].

Pioneering work in utilizing cadmium and lead chalcogenide NC particles as radiation detectors were done at the University of Michigan[33]. This group demonstrated that CdTe and PbSe NC film-based radiation detectors are capable of room temperature detection of α and γ radiations However, poor charge transport in the NC film arising due to insulating long chain stabilizing ligands and poor assembly of the NC. Both of these issues are major impediments that has to be overcome in order to realize commercial grade NC radiation detectors.

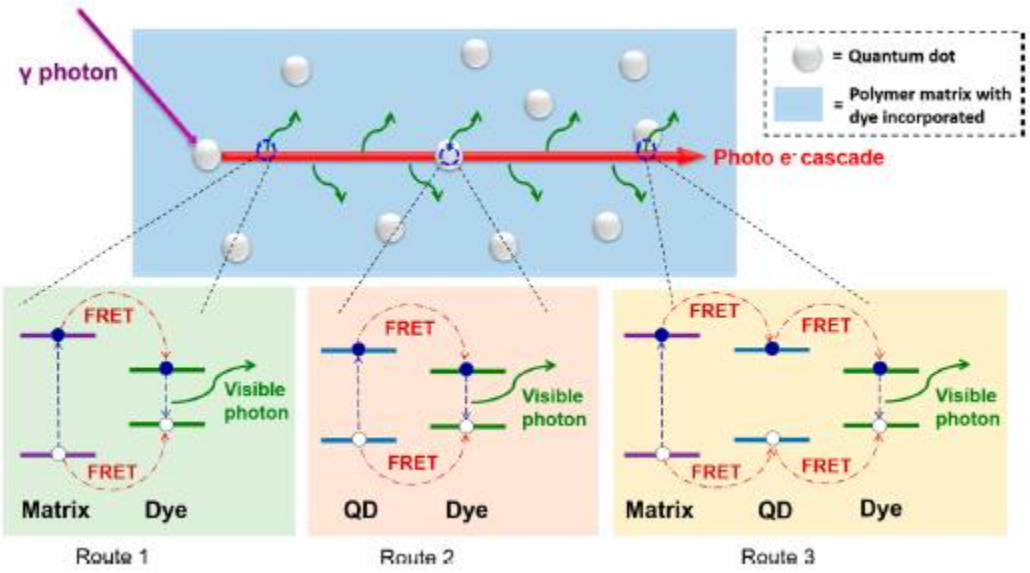

Fig 5. A schematic representation of the scintillation process and FRET routes in a QD/dye/polymer matrix. Reprinted with permission from (C. Liu, "Transparent Ultra-High-Loading Quantum Dot/Polymer Nanocomposite Monolith for Gamma Scintillation," *ACS Nano*, vol. 11, p. 6422−6430, 2017). Copyright 2018 American Chemical Society. [32]

In this research, efforts are made to improve the electronic coupling in NC film assembly by incorporating bi-phasic ligand exchange procedures on monodisperse PbSe NCs with optimal band gap and diameter (Chapter 4).

Chapter 2: Field Effect Sensor Fabrication and Characterization

Fabrication of Thin Film Transistor

Standard TFT fabrication consist of three steps:

1. Thin film deposition,

2. Photolithography, and

3. Etching.

Thin Film Deposition

Either chemical or physical deposition techniques can be used to deposit films with the desired electronic properties for thin film transistors (TFT). Chemical deposition techniques employed in the industry are chemical vapor deposition (CVD), plasma enhanced chemical vapor deposition (PECVD) and atomic layer deposition (ALD). A variety of physical vapor deposition techniques are also used including DC/RF magnetron sputtering, thermal or electron beam evaporation, and pulsed laser deposition (PLD). The criteria used to choose the appropriate film deposition techniques include the thin film material, control of electronic properties, processing temperature, deposition rates/uniformity and the final application. For silicon, wet thermally grown oxide (SiO_2) can be used for field isolation whereas dry thermally grown SiO_2 can be used for the gate dielectric. However, high temperatures are required to grow SiO_2. Low processing temperature requirement for many substrates and introduction of high κ dielectric materials like hafnium dioxide, zirconium dioxide and aluminum dioxide has led to the transition to deposition techniques like PECVD and

ALD. These techniques allow the deposition of high quality films that have low gate leakage currents for TFTs. In addition, ALD grown films improve the interface properties between the semiconducting channel and the gate dielectric. For TFT channel material deposition, DC/RF sputtering is often used for oxide semiconductors [34]. Solution based processes like spin coating and dip coating have also been investigated for channel material and dielectric deposition [35] [36].

Magnetron RF sputter deposition

Sputtering is a physical vapor deposition technique. In this technique, high energy heavy ions bombard a target material (eg. IGZO, ITO etc) resulting in the ejection of atoms from the top layer of the target. This process leads to line of site deposition of films on the substrate. Plasma ionization of an inert gas species like argon is the source of sputtering ions. Sputtering is the primary deposition method utilized in this study, namely magnetron RF sputter deposition. Fig 6 provides a schematic of a magnetron RF sputter system.

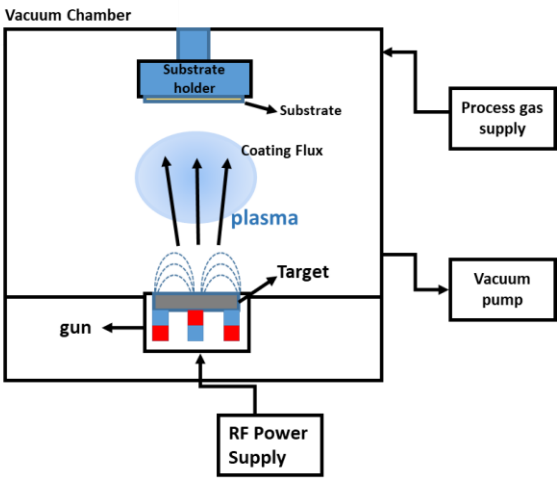

Fig 6. Schematic representation of a Magnetron RF sputter deposition system.

In the most basic configuration, a sputter system is a vacuum chamber with anode and cathode electrodes. An electric field is applied across the electrodes while an inert gas is flowed between the two electrodes. At the breakdown voltage, the plasma ignition occurs as a consequence of electric arc discharge. The target is placed at the cathode such that the accelerating ions hit the target creating a plume of atoms from the target which are deposited on the substrate located in the line of sight of the plume. While DC sputter systems work well with metals, working with dielectrics may lead to charge build-up and arcing issues. Instead, RF or an alternating potential is applied between the electrodes to prevent these issues and allows the deposition of high quality films. However, the deposition rate in RF sputter systems are lower than the DC sputter systems. To increase deposition rates for RF/DC sputtering, permanent or electromagnets can be added to create lines of magnetic flux that are parallel to the target surface. In a magnetic field, the electrons take a helical path around the field lines, causing more electron density near the target. This causes an increase in ionization collisions of the neutral gas species. Thus, the magnetic flux concentrates and intensifies the plasma in the space above the target, resulting in enhanced ion bombardment and sputtering rate in RF sputter systems. In addition to this, using magnetic fields makes it possible to sustain the plasma at lower chamber pressures when compared to conventional sputter systems. However, preferential erosion of target material sometimes referred to as horse track erosion may be a disadvantage to this approach. Although the addition of magnets improves the deposition process, there are other process parameters that interact to achieve the desired film quality at a reasonable deposition rate. These parameters may include, chamber base pressure, process gas pressure and composition, target composition and substrate temperature, RF/DC power, and the distance between the target and the substrate. The film morphology including film quality, roughness, film density, impurity level etc. are a consequence of these process parameters.

In this study, an Orion V magnetron based RF sputter system from AJA International was used to deposit IGZO films. This system is shown in Fig 7.

Fig 7. Orion V sputter system at MASC, Oregon State University

Photolithography and Etching

Photolithography is a process used in microfabrication to pattern parts of a thin film or the bulk of a substrate. It uses light to transfer a geometric pattern from a photomask to a light-sensitive chemical photoresist on the substrate. A series of chemical processes either removes the material not covered by the resist or enables the deposition of a new material in the locations not covered by the photoresist. The ability to project a clear image of a small feature onto the wafer is limited by the wavelength of the light that is used, and the ability of the reduction lens system to capture enough diffraction orders from the illuminated mask. Thus, the two fundamental

relationship that describes a lithography imaging system are resolution (RES) and depth of field (DOF).

$$RES = k_1.\frac{\lambda}{NA} \qquad\qquad DOF = k_2.\frac{\lambda}{(\mathrm{NA})^2}$$

λ is the wave length of the incident light and NA is the numerical aperture of the lens. k_1 and k_2 are empirical constants that relate to the desired critical dimension (CD) control in an integrated circuit manufacturing process [37].

An overview of the thin film fabrication process used in this study is shown schematically in Fig 8. Blanket ITO film was deposited using Magnetron RF sputter deposition process on a 1" x 1" Si substrate with thermal oxide (TO_x). A positive photoresist is spin coated on the ITO blanket film for source and drain patterning. A positive photoresist, when exposed to UV radiation becomes soluble in a developer solution. Therefore, the substrate with the photoresist spun on ITO is exposed to UV radiation, where a photomask defines regions where the source and drain are patterned. After exposure, a chemical developer is used to remove the resist from the exposed region, leaving a resist pattern of the source and drain on the ITO film. The substrate was then immersed in a dilute hydrochloric acid bath where all the ITO film not covered by photoresist etches away revealing the TO_x film surface. Removing the remaining resist reveals the patterned ITO source and drain. Now the IGZO blanket film is deposited on the substrate and the above described process is followed to pattern the channel for the TFT.

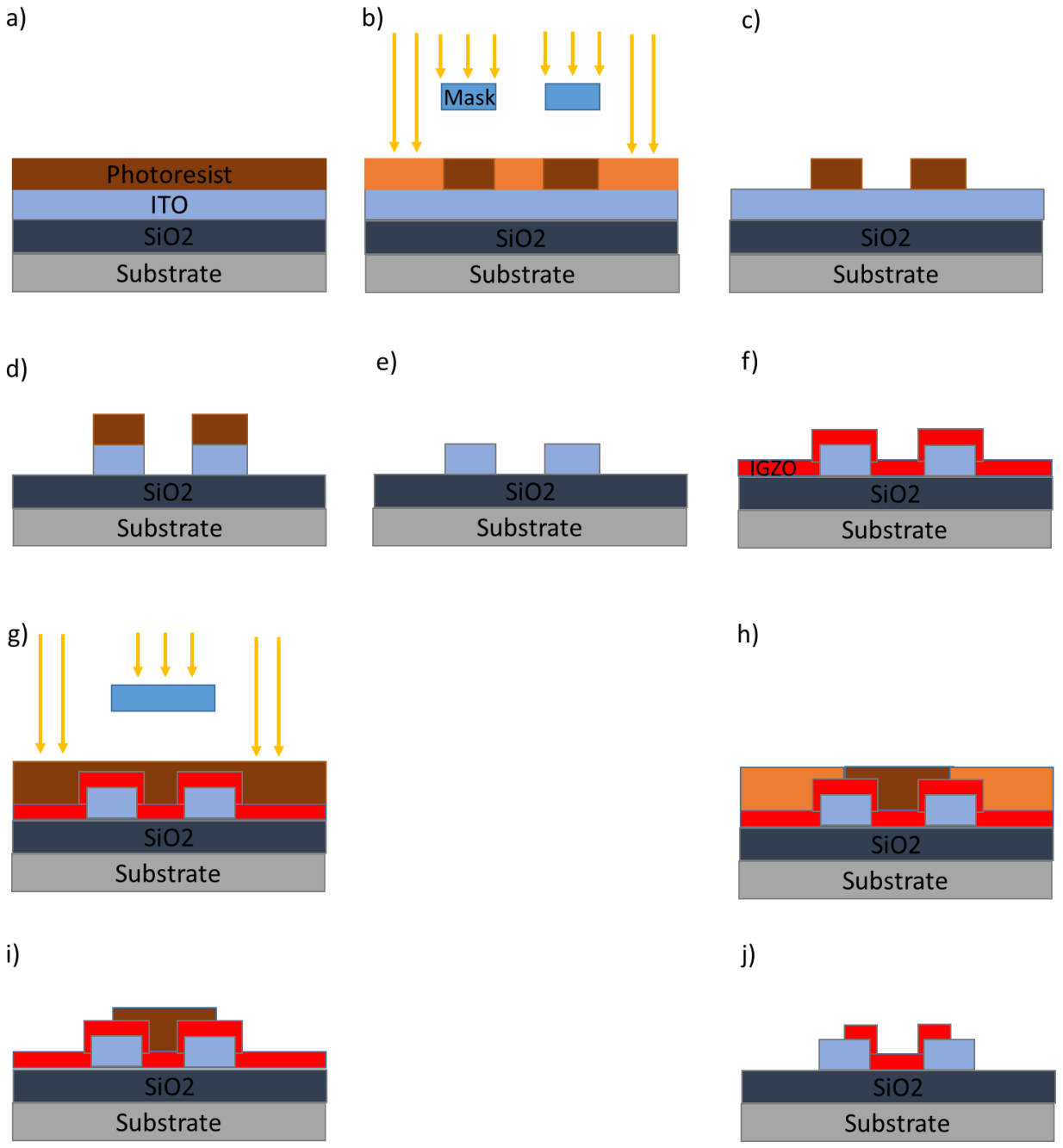

Fig 8.The process flow for a TFT fabrication using photolithography and wet etching a) Positive photoresist is spin-coated onto ITO/TOX substrate. b) Source and drain geometry masked from UV exposure. c) Solubility change in photoresist, soluble regions removed using developer. d) Exposed regions are etched. e) Photoresist stripped leaving source and drain pattern in thin film. Steps g-j depict the deposition and patterning of the IGZO channel similar to the ITO source and drain patterning process.

Semiconductor Parameter Measurements

Electrical measurements for TFTs are measured using a semiconductor parameter analyzer (SPA) and a probe station. SPA is a test instrument that performs multiple measurements and analysis capabilities to perform current-voltage (I-V) and capacitance measurements. In this thesis, we are primarily interested in I-V measurements from TFTs. An Agilent 4155C system was used to measure the I-V data for these studies. The system allows current measurements to be performed down to pA (pico amp) level. A probe station provides structural support for the test bench and facilitates the accurate positioning of the test probe tips utilizing micromanipulators. Test probe tips are usually made of tungsten. An attached microscope is used for placement of the probes and to ensure contact between the electrodes. When the TFT device is electrically biased, the current acquired are displayed on a source measurement unit (SMU). The positioning of the probes on the TFT source, drain, and gate electrodes is shown in Fig 9. I-V measurements are generally performed in a dark environment in order to eliminate the photon-induced current instabilities.

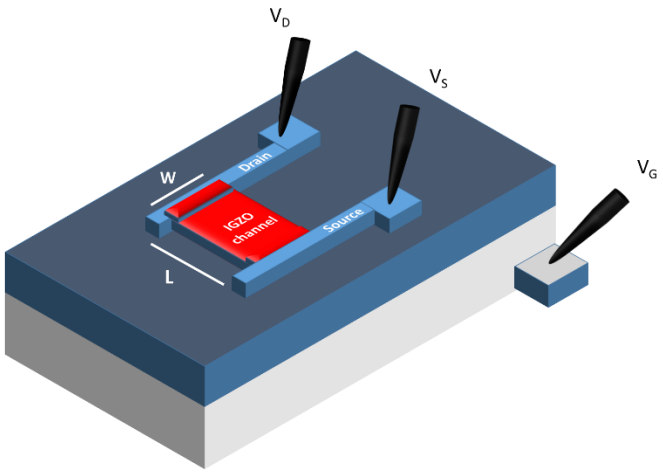

Fig 9. Positioning of the tungsten probe at the gate, source and drain electrodes on a TFT.

TFT Parameter Extraction

Transfer characteristics of a TFT are obtained by setting the drain-source voltage (V_D) to a constant value and simultaneously varying the gate-source voltage (V_G) while measuring the drain current (I_D). The I_D is plotted against V_G. Since the current through the TFT is a function of the channel geometry, I_D is normalized to the (width (W) and length (L)) in order to retrieve the intrinsic properties of the TFT and to facilitate comparison with TFTs of other geometries. A typical normalized transfer curve for an n-type TFT is depicted in Fig 10. The TFT parameters that can be extracted from the transfer characteristics include field effect mobility, sub-threshold swing, turn on voltage, and on and off current (I_{on}/I_{off}).

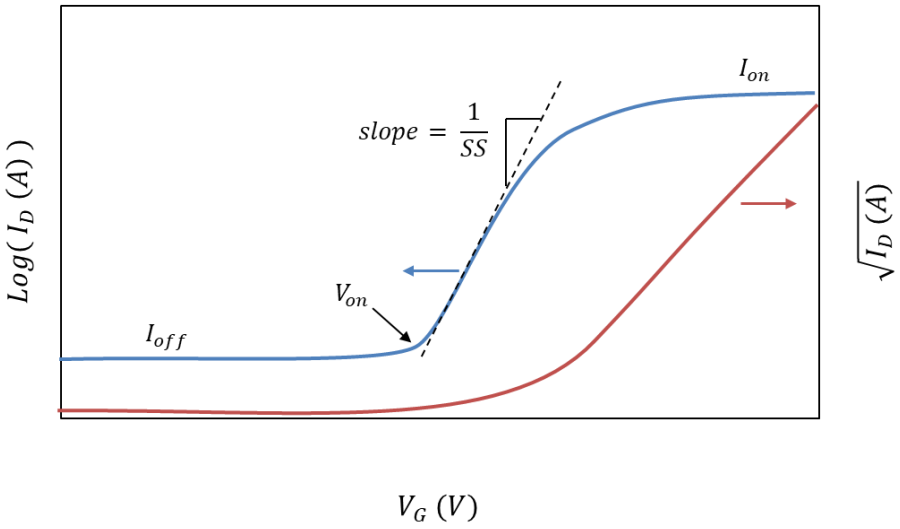

Fig 10. Typical TFT I-V characteristics plot for n-type TFT.

TFTs can operate in depletion or accumulation mode. For depletion mode operation, a V_{ON} ($V_g < 0$) is required to turn off n- channel TFT. For accumulation mode operation a positive ($V_g > 0$) is required to turn on n – channel TFT. Depletion (accumulation) mode devices have (do not have)

mobile charge carriers in the semiconducting channel even when no gate voltage is applied. Based on the polarity of the applied potential, we can either deplete or enhance the channel conductance. When the carrier concentration is enhanced by the applied gate voltage, additional carriers are induced into an accumulation layer at the gate dielectric-semiconductor interface. Thus both carriers in the bulk and interface can contribute to the current in TFTs [38].

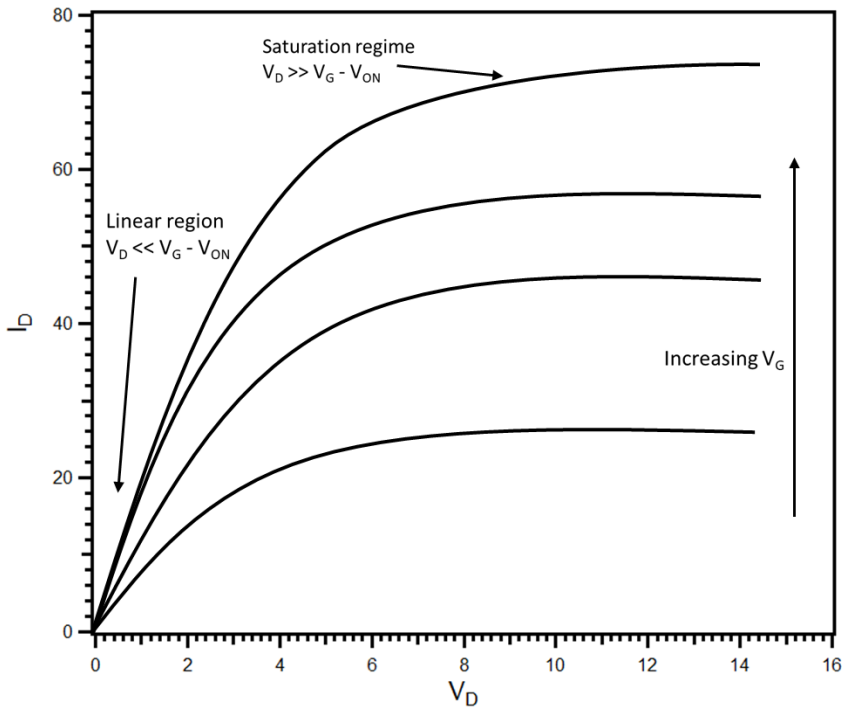

Fig 11. Typical output curve for an n-type TFT. Linear and saturation regimes are labelled Reprinted with permission from (A.P.P. Correia, *A Second-Order ΣΔ ADC Using Sputtered IGZO TFTs*. Springer, 2016).Copyright 2016 Springer Nature.

In the linear regime (Fig 11) for a TFT, the drain current I_D, when $V_D << V_G - V_{ON}$ is by given by [39]:

$$I_D = \frac{W}{L}\,\mu_{lin}\,C_g\,V_D(V_G - V_{on})$$

where, μ_{lin} is the linear regime mobility and Cg is the capacitance of the gate dielectric. In this equation, please note that V_{ON} is used instead of $V_{th.}$ V_{th} is conventionally used in the context of ideal MOSFETs, however V_{th} cannot be accurately measured for the onset of I_D in non- ideal amorphous semiconductors like IGZO [40][41].

Channel Mobility

Channel mobility (μ) is the ease with which the charge carriers in a semiconductor channel are transported under the influence of an electric field. Thus, field effect mobility (μ_{FE})is a measure of the TFT performance, in terms of the fundamental properties of a given semiconductor [41]. In a TFT,the higher the mobility allows, higher switching speed to be achieved. Average mobility (μ_{avg}) and incremental mobility (μ_{inc}) are used to assess channel properties for TFTs. Average mobility (μ_{avg}) for a TFT, based on channel conductance (G_{CH}) in the linear regime is given by [41]:

$$\mu_{avg} = \frac{L\, G_{CH}}{W\, C_g\, (V_G - V_{on})}$$

Where, G_{CH} is the channel conductance which is defined as the change in drain current divided by the change in drain voltage [41]:

$$G_{CH} = \left(\frac{dI_D}{dV_D}\Big|_{V_G}\right)\Bigg|_{for\ small\ V_D}$$

μ_{avg} physically corresponds to the average mobility of the total carrier concentration in the channel whereas μ_{inc} physically corresponds to the mobility of the carriers that are incrementally

added to the channel as the gate voltage incrementally increases in magnitude [41]. The incremental mobility is based on the differential channel conductance $G_{CH}{}'$ given by [41]:

$$\mu_{inc} = \frac{L\ G_{CH}{}'}{W\ C_g\ (V_G - V_{on})}$$

Differential channel conductance ($G_{CH}{}'$) is the differential change in channel conductance (G_{CH}) with respect to gate voltage (V_G)

$$G_{CH}{}' = \frac{dG_{CH}}{dV_G}$$

I_{ON}/I_{OFF} ratio

I_{ON}/I_{OFF} ratio is described as an important parameter to characterize the TFT performance. In an ideal TFT, this ratio is infinity. However, for a typical TFT, the off current (I_{off}) is the current that is observed while $V_G < V_{on}$. Likewise, I_{ON} is the maximum drain output current reached by the TFT. In effect, the drain current on- to- off ratio largely reflects the dimensions, structural characteristics and electrical properties of a TFT. The channel mobility is often considered the most important electrical parameter in quantifying the TFT performance, in terms of the fundamental capabilities of the semiconductor [41]. However, large I_{on}/I_{off} ratio with very low off currents are desired for a TFT as this to reduces the power consumption of the device [42].

Sub-threshold Swing

Sub-threshold swing (SS) is obtained by taking the inverse of the sub-threshold slope.

$$SS = \frac{dV_{GS}}{d\log_{10} I_D} \text{ [mV/dec]}$$

Thus, SS represents the amount of V_G increase required to obtain an order of magnitude increase in I_D. For a TFT, the relation of the SS to depletion capacitance (C_D), trapped interface capacitance (C_{IT}) and gate capacitance (C_g) is described as [42]:

$$SS = \left(\frac{k_B T}{e}\right) \ln(10) \left(1 + \frac{C_D + C_{IT}}{C_g}\right)$$

Where k_B is Boltzmann's constant, e is the elementary charge, C_g is the gate capacitance, and T is the temperature. Assuming that C_D is negligible for a fully depleted channel and replacing $C_{IT} = eD_{sg}$, the equation for SS can be written as a function of trap density$\left(D_{sg}\right)$ in the band gap at the Fermi level.

$$SS = 59.5\left(1 + \frac{eD_{sg}}{C_g}\right)$$

Based on this equation, a lower SS corresponds to lower trap densities and thus a higher quality TFT [42].

TFT based Sensors

The electrical properties of an amorphous oxide semiconductor (AOS) like IGZO and ITO are highly sensitive to their environment. These sensitivities can be leveraged for chemical and biomolecule sensing at the immediate vicinity of the TFT [23]. For a TFT based sensor, the interaction of the analyte can occur at the backchannel surface. When the backchannel of the TFT is functionalized with an analyte-specific molecule (eg., enzyme), the TFT becomes a biosensor that is selective to a particular compound (eg., lactase, urea, glucose). Fig 12 shows a schematic representation of a TFT based biosensor.

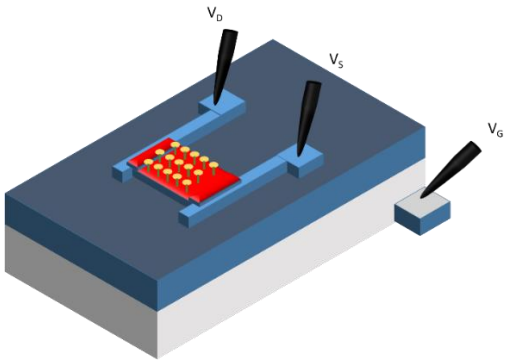

Fig 12. TFT based biosensor. The backchannel of the TFT is functionalized with analyte sensitive molecule for selectivity.

Chapter 3: Glucose Sensing using amorphous IGZO Field Effect Transistors

Introduction

Transparent amorphous oxide semiconductors (TAOS), in particular In-Ga-Zn-O (IGZO) has generated much interest owing to their high mobility and transparency [43] . The room temperature processing compatibility of these materials have opened avenues for integrating them into next-generation electronics on flexible substrates [44]. Currently, IGZO is a mature technology and have been realized in the commercial display industry [45]. Compared to conventional amorphous Si:H thin film transistor (TFT), IGZO TFT devices exhibit low power consumption, low noise and have higher mobility, which translates to higher resolution and faster refreshing rates in flat panel display [46]. The sensitivity of the IGZO channel to ambient environment can be leveraged to develop gas sensors and biomolecule sensors [46][47]. IGZO sensors capable of detecting pH, ammonia, H_2 and NO have been demonstrated [47]. The mechanism of instability of IGZO TFT under varied stresses and illumination need to be understood in order to develop reliable sensors. Instabilities in IGZO TFTs are attributed to charge trapping in the gate dielectric, in the bulk channel, at the channel/insulator interface, at the back channel surface, and deep acceptor traps [48]. Instability reduction strategies may include thermal annealing and back channel passivation [49]. Passivation with self-assembly monolayer (SAM) have shown improved the performance for IGZO TFTs as well as reduced instabilities due to bias stress and the interaction of O_2 and H_2O on the back channel surface [50]. In addition, the IGZO channel can be made sensitive to particular biomolecule by linking an analyte-specific binder to the SAM tail groups [23] . In this chapter, the functionalization of IGZO TFT with glucose oxidase is studied for glucose sensing applications.

The overall idea is to make a platform capable of sensing multiple biomarkers using an array of TFTs on flexible substrates with high repeatability and redundancy.

IGZO Electronic Structure and Charge Transport

For AOS, including IGZO, the electron mobility is not highly sensitive to the crystal structure [48]. That is the mobility in IGZO is not affected whether the film is amorphous or crystalline. This is in contrast to Si, where the mobility can reduce by two orders in magnitude in an amorphous state compared to the crystalline phase [48]. Carrier transport in Si, which is a covalently bonded materials like Si consists of sp^3 hybridized states with strong directivity [44]. Thus, strained and broken Si-Si bonds as in the case of amorphous Si: H lead to localized band tail states and deep gap states which reduce carrier mobility [49]. On the contrary, the electronic structure of IGZO is strongly ionic, in which charge transport happens between metal cation and oxide anion (Fig. 13 a) resulting in a Madelung potential (Fig. 13 b), with the empty s-states of metal cation forming the conduction band minimum (CBM) and the oxygen anion forms the valence band maximum (VBM). Since the conduction band is based on non –directional ns orbitals, the overlap of s orbitals allows IGZO and other AOS materials to have high electron mobility comparable with their crystalline counterparts[51]. Schematic orbital drawings for carrier transport paths in crystalline and amorphous semiconductors are shown in Fig. 14.

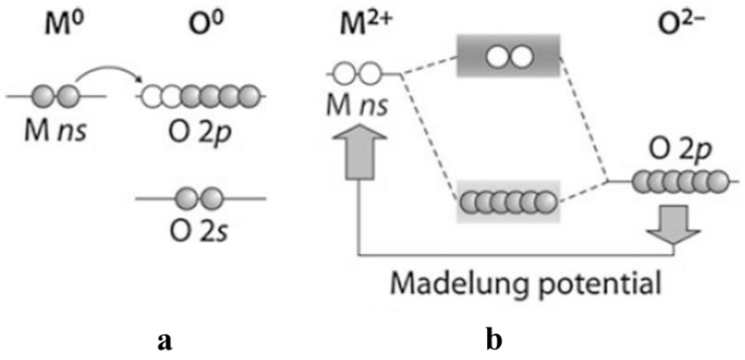

Fig 13. Schematic diagram of a) charge transfer in AOS b) Madelung potential in AOS. Reprinted with permission from (T. Kamiya and H. Hosono, "Material characteristics and applications of transparent amorphous oxide semiconductors," *NPG Asia Mater.*, vol. 2, no. 1, pp. 15–22, 2010). Copyright 2010 Springer Nature.

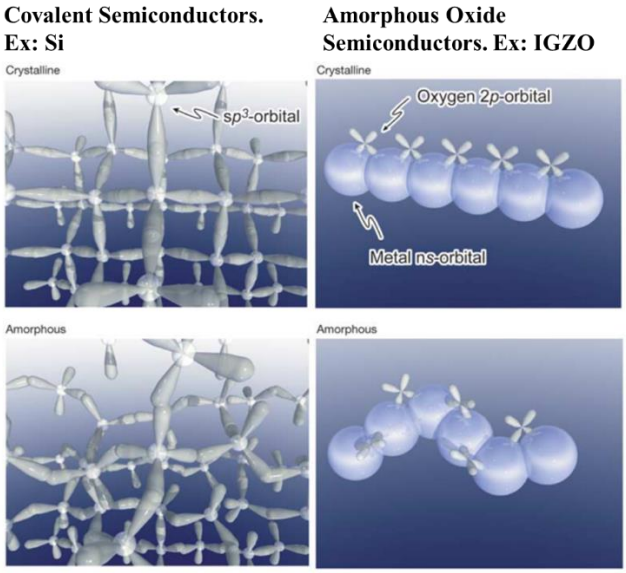

Fig 14. Schematic orbital drawings for carrier transport paths in crystalline and amorphous semiconductors. Reprinted with permission from (K. Nomura, H. Ohta, A. Takagi, T. Kamiya, M. Hirano, and H. Hosono, "Room-temperature fabrication of transparent flexible thin-film transistors using amorphous oxide semiconductors," *Nature*, vol. 432, pp. 488–492, 2004). Copyright 2004 Springer Nature.

Doping of IGZO and other AOS materials is achieved by adjusting the oxygen vacancies in the material [49]. The oxygen vacancies in IGZO creates a non-bonded metal cation forming shallow donor levels. It can be controlled by optimizing the oxygen partial pressure during deposition of IGZO films. A higher concentration of oxygen vacancies increase the free carrier density. Thus films deposited in lower oxygen partial pressure results in a higher concentration of charge carriers [49]. The reversible increase of free electron concentrations due to prolonged exposure to vacuum has also been reported [49]. Low-temperature annealing of IGZO in an H_2-N_2 environment also increases free carrier concentrations [49]. However, higher charge concentration is not necessarily desirable for a TFT because it will result in higher off currents which is not desirable for display or sensor applications. As mentioned above, the carrier concentration can be decreased by increasing the oxygen partial pressure during deposition, or by annealing in an O_2 environment.

In IGZO films, the mobility increases as the charge carrier density increases [49]. This is attributed to percolation limited transport within the conduction band. This is in contrast to Si: H where higher charge densities decrease mobility due to charge scattering and increased charge impurity. At moderate doping levels, thermally activated mobility increase is observed in IGZO films until doping levels of 2×10^{18} cm^{-3}, and after which the mobility is temperature independent [49] . This temperature dependent mobility is explained by percolation theory. According to this theory, a longer conduction path corresponding to the lowest energy pathway is adopted by the charge carriers at low temperatures. Whereas in case of high temperatures, the charge carriers have enough energy to overcome high barriers and adopt shorter conductive pathways enabling higher mobility [52].

Density of localized Gap State (DOS)

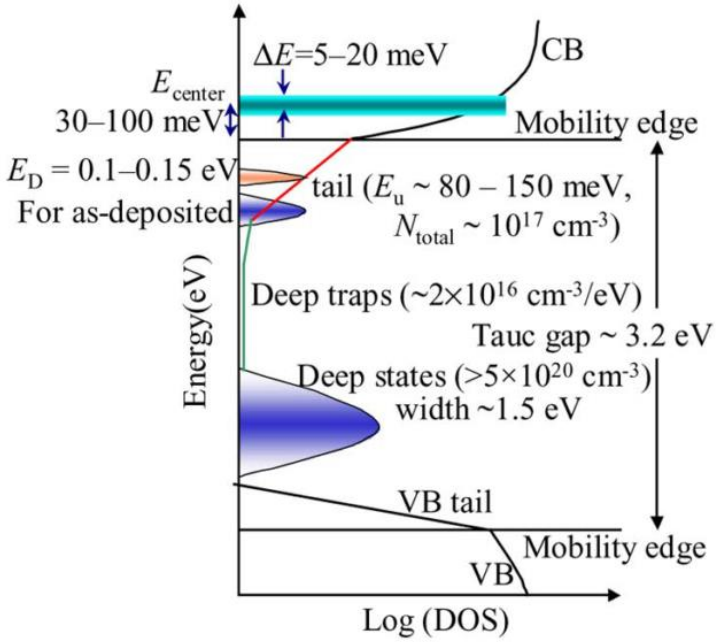

Fig 15. Summary of density of states in IGZO. Reprinted with permission from (T. Kamiya, K. Nomura, and H. Hosono, "Origins of High Mobility and Low Operation Voltage of Amorphous Oxide TFTs: Electronic Structure, Electron Transport, Defects and Doping*," *J. Disp. Technol.*, vol. 5, no. 12, pp. 468–483, 2009). Copyright 2009 IEEE.

Understanding the density of localized gap states (DOS) is very important to improve the TFT characteristics like mobility and SS [43]. These states exist between valence band maximum (VCM) and conduction band minimum (CBM) and act as charge carrier traps leading to decreased device performance [42]. The DOS are determined using capacitance–voltage (C–V) measurements that can be performed on TFTs. This method allows an estimation of trap occupancy as a function of gate bias [49]. For DOS measurements, the C–V method is accepted over the I-V method because the latter assumes that the electron mobility is independent of charge density which is not accurate. The measured DOS for IGZO are one to two orders of magnitude less than a-Si: H, which explains the higher mobility and lower SS in IGZO devices [43]. A schematic of the DOS for IGZO is shown in Fig 15. Based on density functional theory, it has been determined

that a fully occupied deep donor level located around 1.0 eV above the VBM is formed by oxygen vacancies (V^0_O) [53]. These oxygen vacancies trap and prevent the electrons from partaking in conduction [53]. These deep states near the VBM have a higher density than the holes generated by the gate voltage and is the reason that p-type IGZO does not exist [53].

IGZO Instabilities

For commercial IGZO based devices, the stability are characterized under different stressors: i) illumination, ii) bias stress and, iii) mechanical stress [48]. It has also been shown that channel surface/ambient interactions are of paramount importance in regards to device stability [48]. The instability may include a shift in the threshold voltage in the positive or negative direction accompanied by minimal changes in mobility and subthreshold slope [48]. Under optical illumination, a threshold voltage shift would happen in both above band gap illumination (365nm) as well as the subgap illumination (460 nm). Although the bandgap illumination has a higher effect on IGZO TFT for transparent sensor applications, the shift due to subgap band illumination is an important issue that must be addressed [49]. Filtering light to remove wavelengths below 430 nm has been achieved in the display industry without compromising display performance [48]. This may be a solution for overcoming subgap illumination based instability in IGZO based transparent sensing platforms. In the metal–semiconductor field-effect transistor (MESFET) configuration, optical based illumination instabilities were greatly reduced by using silver-based Schottky gates [54]. The increased stability was attributed to the charge trapping at the gate- channel interface. High-pressure annealing of IGZO TFT in an O_2 ambient have shown improvements in negative bias stress illumination stress (NBIS) stability due to the reduction of oxygen vacancies [55].

Passivation of the back channel of IGZO TFT has also helped to reduce the instabilities in IGZO TFT [48]. Instability effects under both negative and positive gate bias instabilities are reported for IGZO TFTs. Positive bias instability where the threshold voltage shifts positively are attributed to electron trapping at the IGZO/ dielectric interface while negative bias instability is attributed to hole trapping [56][57]. Thermal annealing IGZO TFTs have resulted in improved device performance, as well as reduced instabilities [49]. In addition, optimized processing conditions/techniques for the channel, gate dielectric and interface can also lead to improved bias stability [58]. Improvements in the voltage stability for IGZO TFTs has been demonstrated by insertion of a thin interfacial layer (SiN_x) between atomic layer deposited (ALD) gate dielectric (Al_2O_3) and IGZO channel [48]. Instabilities in IGZO performance can also be due to the ambient/backchannel interaction. Interaction of the IGZO back channel with O_2 and H_2O can lead to surface depletion and donor-like surface states respectively [59]. The IGZO surface is sensitive to other molecules like ethanol, NO_2, H_2 [47][59]. This sensitivity stems from the fact these gas molecules alter the carrier density at the back channel and changes the IGZO conductivity. When tracked systematically, these changes can be correlated to the concentration of these gas species in the ambient [59]. The instabilities due to O_2 and H_2O can be controlled by adding a passivation layer on top of the IGZO to prevent the interaction of O_2 and H_2O with the back channel. The passivation of the IGZO back channel with self-assembly monolayer (SAM) like n-hexylphosphonic acid (n-HPA) and (3,3,4,4,5,5,6,6,6-nonafluorohexyl) phosphonic acid (FPA) can lead to lower bias stress results. This improved stability was attributed to the reduction of adsorbed molecular species on the channel surface and also to the reduction in trap density due to phosphonic acid binding [50].

Materials and Methods

Materials.

Glucose was obtained from Alfa Aesar. Phosphate buffer saline (PBS) tablets were acquired from Sigma Aldrich. 3-aminopropyltrimethoxysilane (APTMS) and glucose oxidase (GO_x) were bought from TCI America and VWR life sciences, respectively. IGZO (molar composition: In_2O_3:Ga_2O_3: ZnO (1:1:1)) and ITO (composition, In_2O_3: SnO_2 = 90:10 (wt %)) targets have been purchased from Kurt J. Lesker Inc. Sylgard 184 PDMS was obtained from Dow Corning. Double-sided adhesive tape was purchased from 3M. Transparent polycarbonate sheet was purchased from Amazon. Milli-Q water (18.2 MΩ cm) was used in all sample preparation.

Device Fabrication.

IGZO-FET test structures were fabricated using a heavily p-doped Si substrate as the gate and thermally grown SiO_2 (100 nm thick) as the gate dielectric. The substrate was rinsed with acetone, isopropyl alcohol and water prior to processing. ITO films 150 nm thick were deposited using RF magnetron sputter deposition from a 3” ITO target. The process parameters used were 75W RF power, ~5 mTorr chamber pressure, Ar flowrate of 12 sccm, and flowrate of Ar:O_2 (90:10) mixture of 2 sccm. The source and drain were patterned using photolithography and etched in diluted HCl (1:5 HCl: H_2O) giving a width/length (W/L) ratio of 5. Amorphous IGZO films (50 nm thick) were deposited by sputtering, 75W RF power, ~5 mTorr chamber pressure, and 18/1 sccm flowrate for Ar/ O_2 gas. IGZO active layers were patterned using photolithography and were etched using dilute HCl (1:200 HCl: H_2O).The thin film transistor test structures were subsequently annealed in the air to 300 °C for 1 hour to improve the electrical properties and stability. The device is then

sonicated for 15 mins in acetone, followed by IPA, DI water rinse and dried using N_2. Backchannel surface passivation was performed by activating and cleaning the IGZO surface using an UV-Ozone (Novascan Technologies, Inc.) treatment for 15 minutes, which was then followed by immediate immersion of the IGZO-FETs in 2% APTMS solution in ethanol. After 24 hours, samples were removed from the solution, rinsed with ethanol, and then dried with flowing nitrogen. The passivated FETs were annealed at 110 °C for 10 mins. The ATPMS-IGZO film was then immersed in 20 mM glutaraldehyde (GA) in a PBS solution for 2 hrs. GA act as a crosslinker for immobilizing glucose oxidase (GO_x) on the IGZO surface. Finally, the device was transferred to 10 mg/ml GO_x – PBS solution for 2 hrs. The device was further rinsed with water and blow dried using N_2.

pH / Glucose Detection.

All IGZO-FET electrical measurements were performed using an Agilent 4155C precision semiconductor parameter analyzer in a dark chamber. Transfer curves were obtained by sweeping the gate voltage (V_G) forward (low voltage to high voltage) and then backward (high voltage to low voltage) with the drain voltage (V_D) set to 100 mV while measuring the drain current (I_D) using a V_G step size of 0.2 V. A microfluidic channel was fixed on top of the device such that the sensing channel surface is exposed to the fluid in the channel. Solutions were introduced into the microfluidic channel via a press tube fit accessory using a syringe, where the pH was varied between 6-8 and glucose concentration was varied between 0-20 mM.

Results and Discussions

Fig 16 compares the N1s X-ray photoelectron spectroscopy (XPS) data obtained from a bare IGZO surface and an APTMS passivated IGZO surface. This XPS spectrum was performed using a PHI PerkinElmer 5600 X-ray photoelectron and Auger electron microscopy system using a dual anode Mg Kα radiation (photon energy = 1253.6 eV). The spectra were acquired with a 45^{o} emission angle and an electron analyzer pass energy of 54.7 eV.

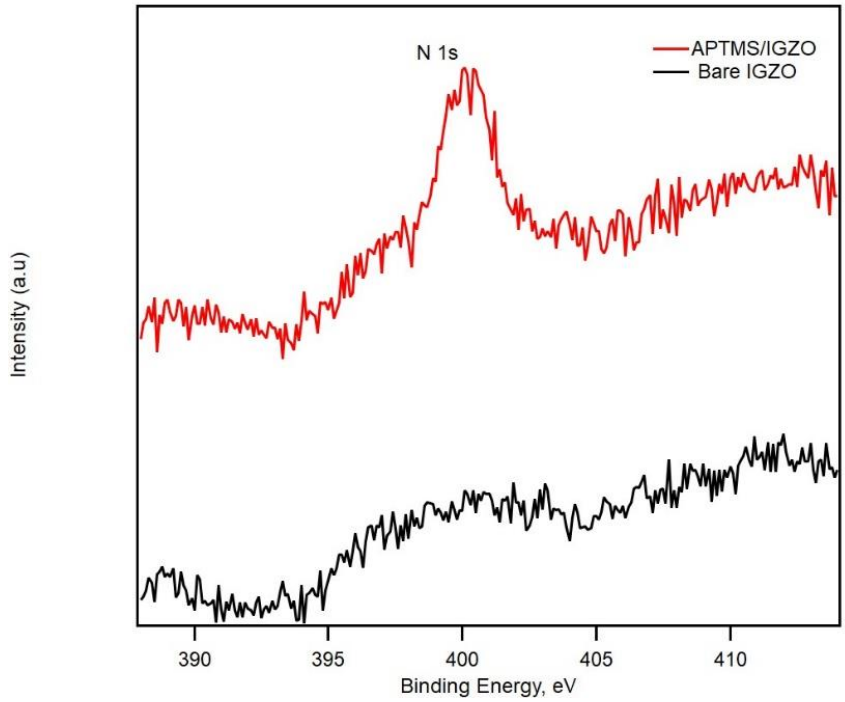

Fig 16. XPS spectra indicating the N1s peak from a bare IGZO surface and the APTMS passivated IGZO surface.

The formation of APTMS self-assembly monolayer on the IGZO surface occurs through a condensation reaction [3]. During solution phase passivation, the APTMS molecules diffuse to the hydroxylated IGZO surface and the reaction between the silane and the OH group on the surface promotes the formation a uniform monolayer of aminosilane with the amine (NH_2) group extending away from the IGZO surface [60][61]. The presence of APTMS can be confirmed by

measuring the N1s peak associated with the NH_2 group. As evident from Fig 15, no N1s peak is observed for the bare IGZO surface. However, after passivation with APTMS, an intense N1s peak was observed indicating the presence of NH_2 at the surface and thus confirming the passivation of IGZO surface with APTMS.

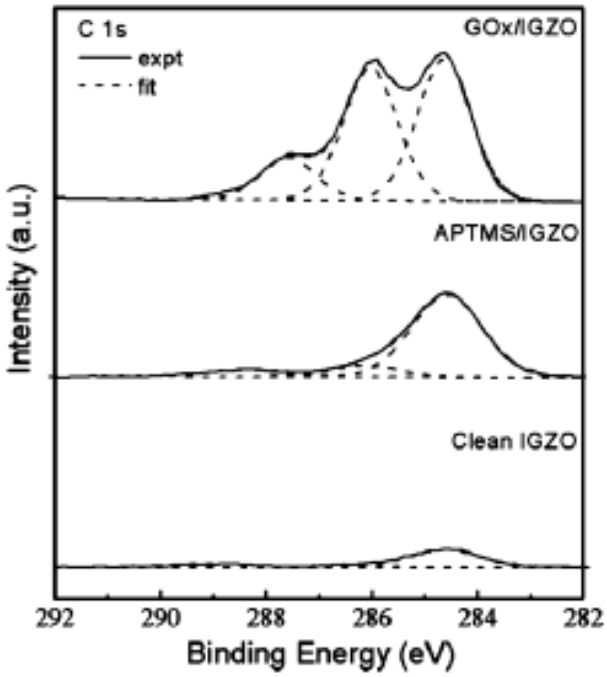

Fig 17. XPS spectra indicating the changes in C1s peak from a bare IGZO surface and the APTMS passivated IGZO surface. Reprinted with permission from (X. Du, Y. Li, J. R. Motley, W. F. Stickle, and G. S. Herman, "Glucose Sensing Using Functionalized Amorphous In–Ga–Zn–O Field-Effect Transistors," *ACS Appl. Mater. Interfaces*, vol. 8, no. 12, pp. 7631–7637, 2016).Copyright 2016 American Chemical Society.

The immobilization of GOx in this study was carried out using a recipe published previously [3]. In the same paper, the presence of GO_x molecules was confirmed using XPS where they attributed the high energy peaks (Fig 17) at 286.1 eV and 287.7 eV to characteristic -C*H_2 - bonded to the peptide linkage groups (-NH-(C=O)-) and peptide groups (-NH-(C*=O)-) in proteins, respectively. These results confirmed the immobilization of GO_x to the IGZO surface [3].

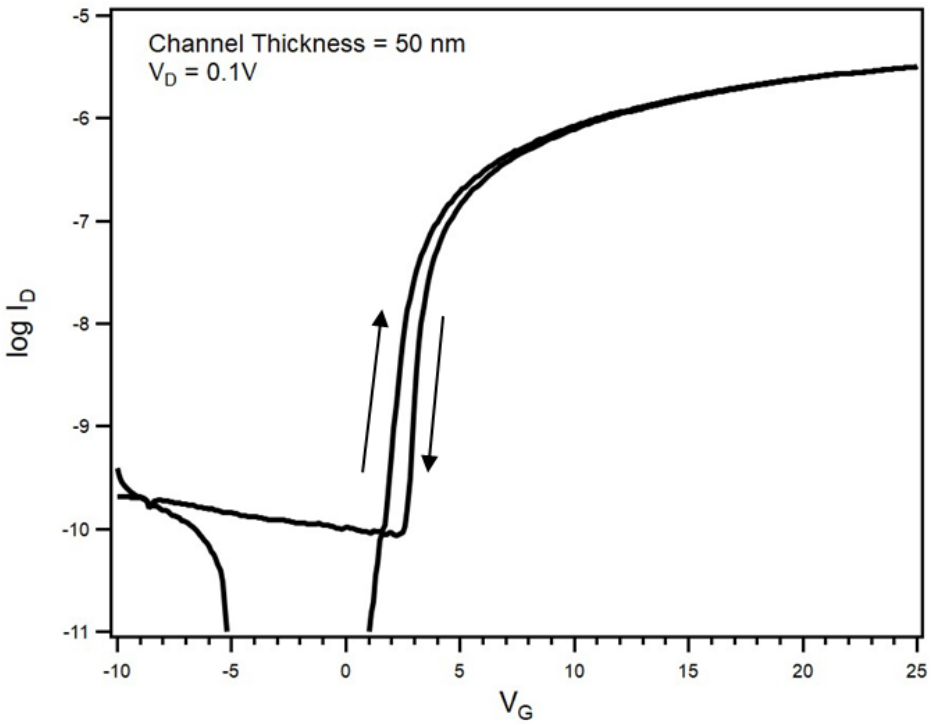

Fig 18. Transfer curve obtained for an IGZO TFT with W/L = 5 after 300ºC anneal.

The optimized transfer characteristics of an IGZO TFT that is suitable for biosensing is shown in Fig 18. The average mobility was determined to be 8.11 cm^2/V.s with a V_{ON} of 1V. However, we were not able to obtain reproducible device performance using the deposition system in the Material Synthesis and Characterization (MASC) facility in spite of repeated efforts. The transfer curves for the IGZO TFTs fabricated in this study, before and after the passivation with APTMS are shown in Fig 19. These measurements were performed in air. The transfer characteristics were obtained by measuring I_D, while sweeping the gate voltage V_G from -10 V to 25 V and back down to -10 V with a constant drain voltage V_D of 0.1 V. The TFT parameters like μ_{avg} and V_{ON} were extracted as mentioned elsewhere [41]. The equation used to calculate μ_{avg} is given by

$$\mu_{avg} = \frac{L\, G_{CH}}{W\, C_g\, (V_G - V_{on})}$$

Table 1 provides a summary of these parameters for both passivated and non-passivated IGZO TFTs. As evident from the Fig 19, the transfer curves obtained for the IGZO TFTs had sluggish turn-on even after annealing at 300°C for 1 hr. The μ_{avg} obtained for the non-passivated TFT was 0.17 cm^2/V.s which is considerably less than prior studies [3] and the device results shown in Fig 18. The APTMS passivated IGZO TFT had a slight improvement in average mobility and a negative turn on voltage (V_{ON}) shift to -3.2 V. These results are different than from the literature where APTMS functionalization caused little or no change in the V_{ON} or average mobility [3][13].

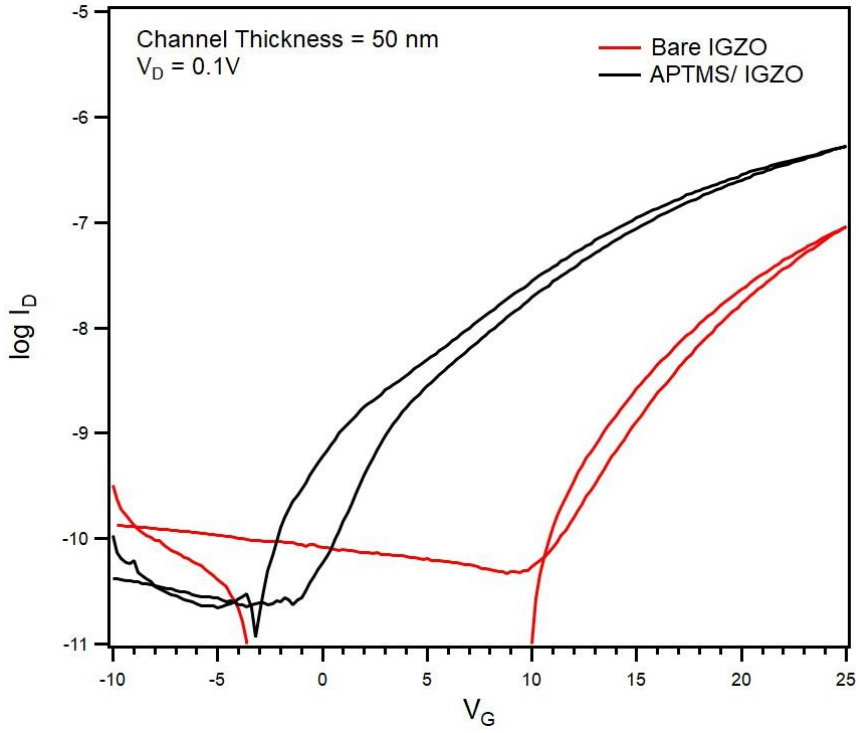

Fig 19. The transfer curves for the IGZO TFT before and after the passivation with APTMS.

Surface treatment	**Avg. Mobility, cm^2/V.s**	**Turn On Voltage (V_{ON}) , V**
Bare IGZO- annealed	0.17	10
APTMS/IGZO	0.68	-3.2

Table 1. The TFT parameters for the IGZO TFT before and after the passivation with APTMS.

A large shift in V_{ON} suggests that the conductance of the IGZO channel is altered after functionalization [13]. The conductance of the IGZO channel may be altered due to the change in carrier concentrations near the semiconductor back channel. The formation of acceptor-like or donor-like states due to adsorption of species like O_2 or H_2O at the back channel surface can lead to band bending thus shifting the V_{ON} [62][63]. It is also possible is that the APTMS functionalization was not uniform in this study. This was also observed for (3-Aminopropyl)triethoxysilane (APTES) when adsorbed on to IGZO surface using a low concentration (1% in ethanol solvent) where self-polymerization in the solvent occurred during passivation [60]. In our experiments a non-uniform APTMS SAM may have exposed portions of the IGZO surface to the ambient which acts as an electron donor resulting in an increase in carrier density and conductivity [63]. The resulting parallel parasitic conduction path at the surface may be the reason for the large negative shift in V_{ON} [48]. This problem of non-uniform monolayer formation in case of APTMS passivation can be averted by switching solution based passivation procedures to chemical vapor deposition procedures which give high uniformity and better coverage for silane self-assembly monolayer [64].

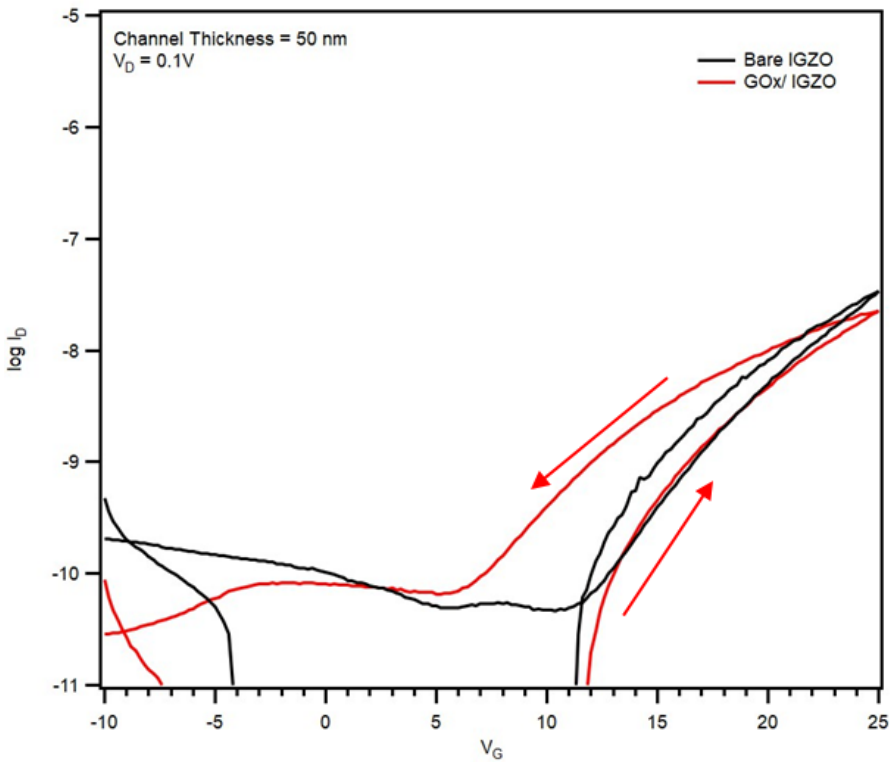

Fig 20. The transfer curves for the IGZO TFT before and after functionalization with GOx.

Surface treatment	Avg. Mobility, cm2/V.s	Turn On Voltage, VON
Bare IGZO- annealed	0.07	11.2
GOx/IGZO	0.05	11.8

Table 2. The TFT parameters for the IGZO TFT before and after functionalization with GOx.

Fig 20 shows the transfer characteristics for the IGZO TFT before and after the functionalization with GOx. The extracted TFT parameters show poor electrical performance, however the slight reduction in average mobility and slight positive change in V_{ON} post-GOx immobilization was previously reported [3]. After immobilization of GO_x on IGZO TFTs, we observe counterclockwise hysteresis compared to the typical clockwise hysteresis [13]. Clockwise hysteresis in IGZO TFTs is attributed to the charge trapping at the gate oxide /IGZO interface by shallow energy defects [65]. In order to achieve the same carrier density in the channel between sweeping V_G up or down a higher V_G is required to turn the device off. The counter-clockwise

hysteresis observed in our study can be attributed to the mobile charge carriers and the electrical dipole movements [65]. Prior studies have determined that H_2O at the channel/dielectric interface can act as electric dipoles which provide extra electric fields at the interface which results in a negative V_{ON} shift [65]. The source of H_2O for our devices may be from the ambient or from the solvents used for functionalization (ethanol, PBS).

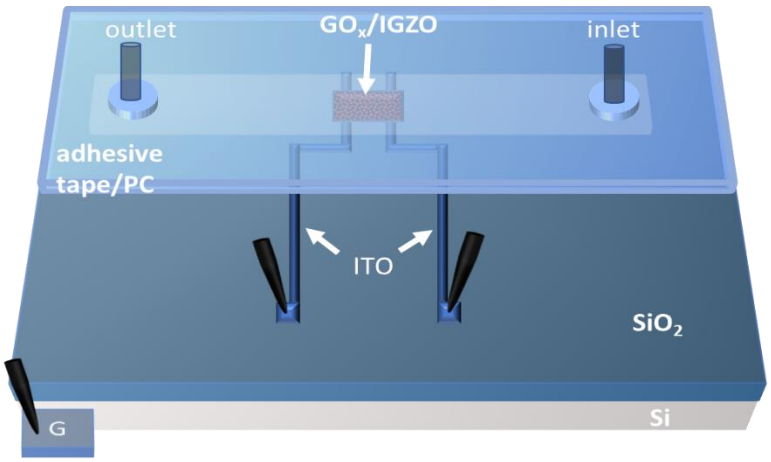

Fig 21. Schematic of the experimental setup used for IGZO sensors.

Fig 21 is a schematic representation of the device structure used for sensing, where a channel defines the contact area for the analyte solution and the backchannel of the IGZO TFT. To make the fluidic setup, the dimension of the channel were laser cut on a double-sided 3M adhesive tape. This was fixed on the substrate such that the TFT back channel is exposed. A transparent polycarbonate sheet cut in the dimension of the adhesive tape is fixed on the top of the substrate such that the exposed channel is sealed. Inlet and outlet holes were carefully drilled to allow fluid delivery inside the channel.

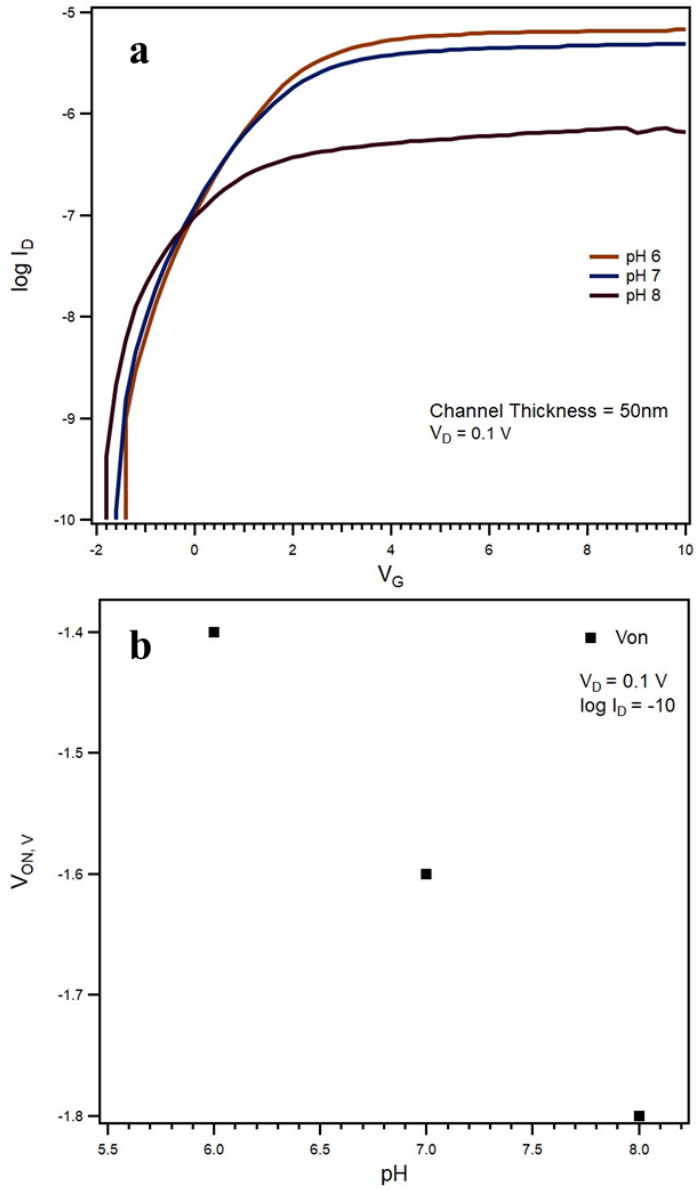

Fig 22. The transfer curves for APTMS functionalized IGZO TFT after exposure to varying pH. b. Change in V_{ON} for varying pH concentrations.

Initial measurements were carried out on an APTMS functionalized IGZO TFT where the pH of PBS solution was varied from high to low values. In Fig 22 a we show transfer curves for an APTMS functionalized IGZO TFT at 3 different pH values. Compared to measurements performed in air (Fig 19), we find an increase in the saturation current and a much lower sub threshold swing (SS). This can be due to the increase in charge carriers in the IGZO channel when in contact with the PBS solution [66]. When pH of the solution was varied, we observed that the V_{ON} shifts

positively for lower pH values and shifts negative for higher pH values. Fig 22 b shows the change in V_{ON} for varying pH values for a set I_D.

The mechanism behind this reversible V_{ON} change can be attributed to the protonation of the $–NH_2$ group and deprotonation of the –OH groups at the IGZO surface, respectively for low and high pH environments [3] [67]. At lower pH, the excess H^+ ions protonate the $–NH_2$ groups to $–NH_3^+$ which results in positively charged surface. On the contrary, at higher pH environments, the –OH group on the surface is deprotonated to $–O^-$ making the surface negative [67]. Therefore at lower pH, an acceptor-like state is formed on the IGZO surface that can deplete the charge carriers in the channel, which leads to a positive shift in V_{ON}. Likewise, at higher concentrations, a donor like state on the IGZO surface can inject charge carriers into the channel, which leads to a negative shift in V_{ON}. A schematic representation of the variation in surface states on IGZO with changing pH is given in Fig 23.

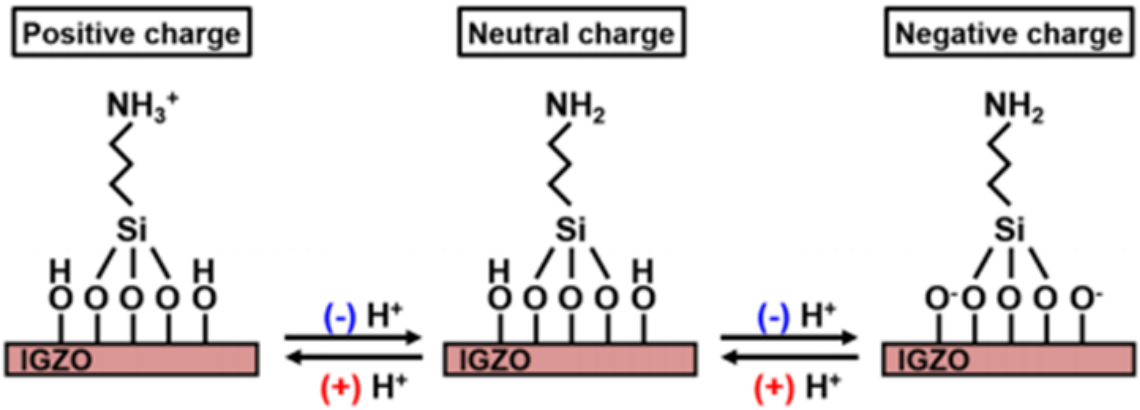

Fig 23. Schematic illustration of pH sensing mechanism on APTMS passivated IGZO TFT. Reprinted with permission from (Y. G. Kim, Y. J. Tak, H. J. Kim, W. G. Kim, H. Yoo, and H. J. Kim, "Facile fabrication of wire-type indium gallium zinc oxide thin-film transistors applicable to ultrasensitive flexible sensors," *Sci. Rep.*, vol. 8, no. 1, pp. 1–7, 2018). Copyright 2018 Nature.

The transfer curves obtained for GOx functionalized IGZO TFT for different glucose concentrations (1-20mM in PBS solution) is shown in Fig. 24 a. A positive shift in V_{ON} was observed for increasing glucose concentrations. A plot of V_{ON} versus log concentration shows a linear relationship for the glucose concentrations in the range of 1-20mM as shown in Fig 24 b.

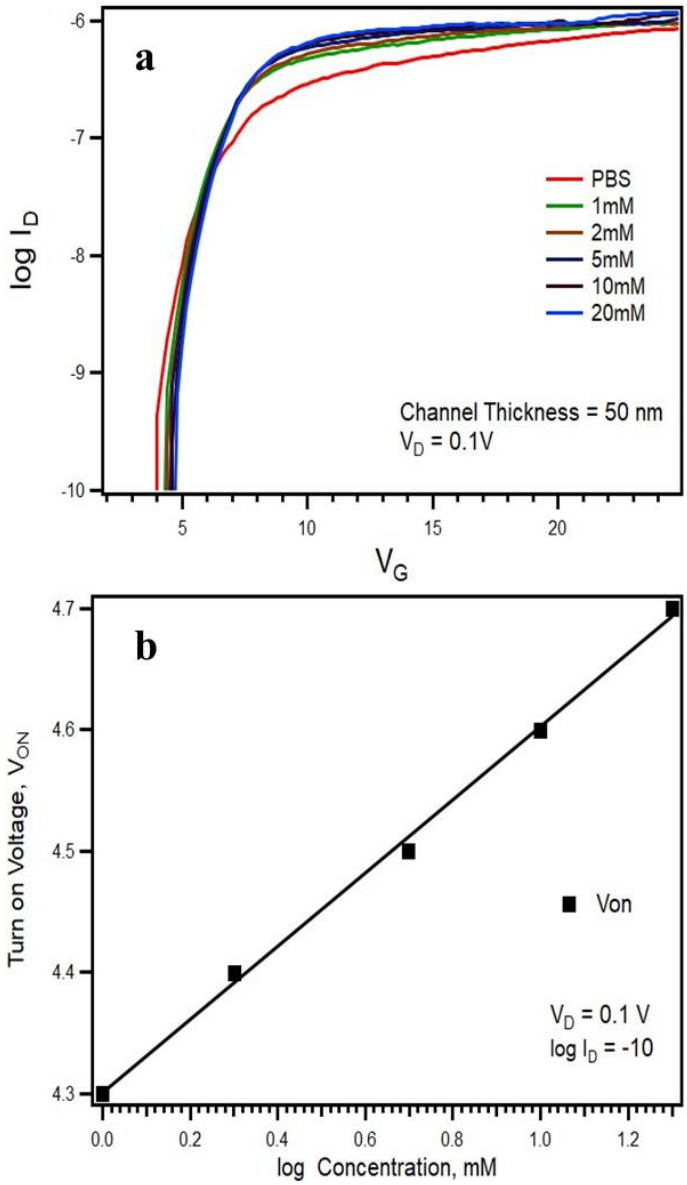

Fig 24. The transfer curves for GOx functionalized IGZO TFT for varying glucose concentrations. b. Change in V_{ON} for varying log of glucose concentrations.

The shift in V_{ON} is attributed to the bio-catalytic oxidation of glucose to gluconic acid in the presence of glucose oxidase, which alters the acidity at the IGZO/electrolyte interface [13][68]. The glucose oxidation reaction catalyzed by GOx is shown in Fig 25.

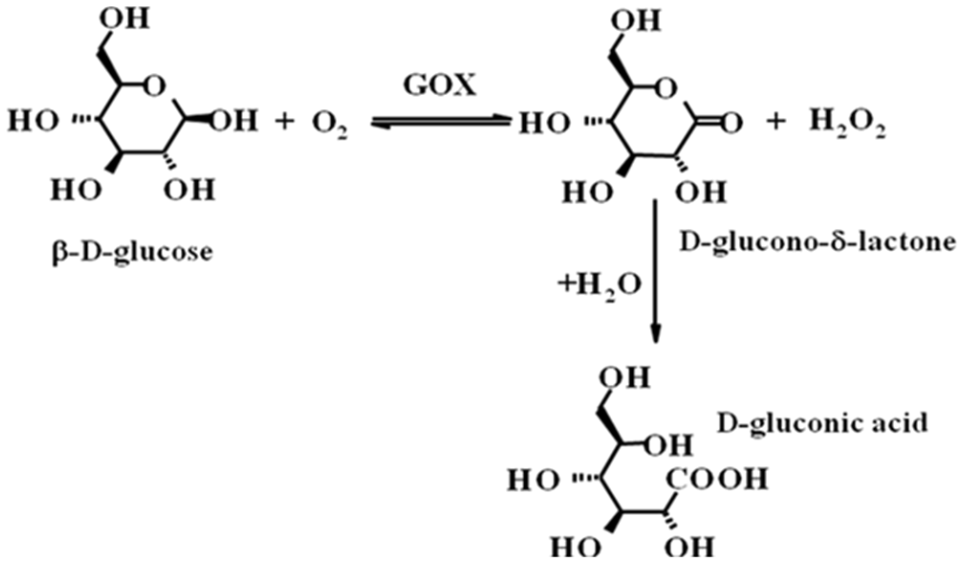

Fig 25. Biocatalytic oxidation of glucose to gluconic acid in the presence of GOx. (Image from https://www.tankonyvtar.hu/en/tartalom/tamop425/0011_1A_Proteinbiotech_en_book/ch14.html)

The generated protons lower the pH at the vicinity of the aminosilane molecules, which results in the protonation of the $–NH_2$ group. This creates acceptor-like states on the surface as explained previously [13]. The accumulation of electrons close to the a-IGZO back-channel surface can be depleted by NH_3^+ acceptor-like states, leading to a negative shift in the Fermi energy as schematically shown in Fig 26. This results in more positive V_{ON} for increasing glucose concentrations. Immobilization of GOx molecules on the IGZO surface is imperative to provide selectivity and improved electrical response as cited in previous studies on FET based glucose sensors [3][68].

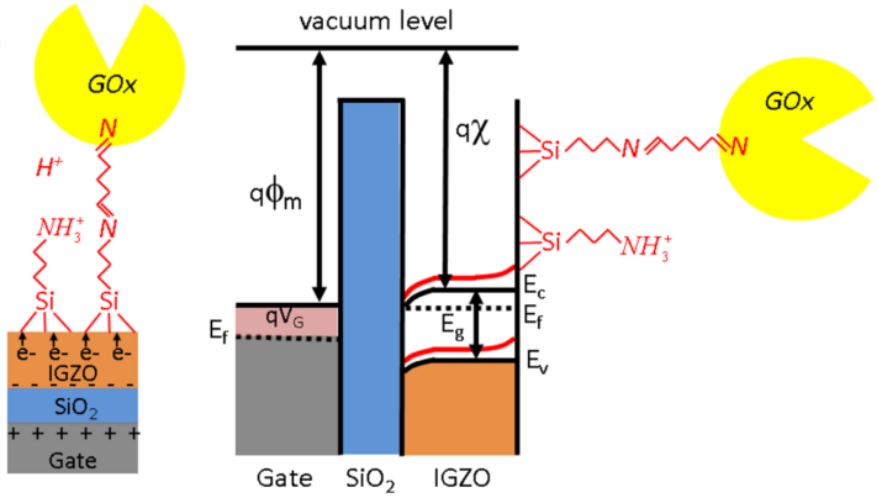

Fig 26. Schematic diagram showing the band bending at IGZO surface due to positively charged aminosilane groups as an electron acceptor. Reprinted with permission from (X. Du, Y. Li, J. R. Motley, W. F. Stickle, and G. S. Herman, "Glucose Sensing Using Functionalized Amorphous In–Ga–Zn–O Field-Effect Transistors," *ACS Appl. Mater. Interfaces*, vol. 8, no. 12, pp. 7631–7637, 2016). Copyright 2016 American Chemical Society.

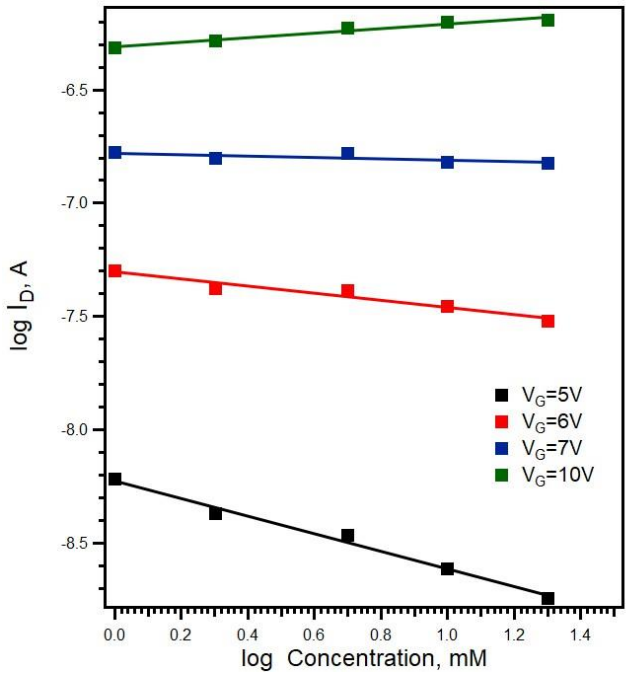

V_G , V	Slope, A/mM	R^2
5	-0.39	0.987
6	-0.16	0.934
7	-0.03	0.584
10	0.1	0.968

Fig 27. log – log plot for concentration verses I_D. The slope and the R^2 value for the different V_G is tabulated.

For continuous glucose measurements, monitoring the change in I_D is done by keeping V_D and V_G constant [68]. For maximum sensitivity, it is important to identify the V_G at which maximum change in I_D occurs. To identify the optimum V_G, a log-log plot of glucose concentration versus I_D is shown for four different V_G values (Fig 27). The data suggest that the maximum sensitivity for the device occurs at V_G=5V, with a slope of -0.39 A/mM and an R^2 value of 0.987. The trend indicates that as we go to more positive V_G the sensitivity decreases as evident in the decrease in the magnitude of the slope until an inversion point occurs after which, the slope starts to increase again. As a result, the optimum V_G for the continuous glucose measurements would be in the regime close to the V_{ON} of the TFT device.

Chapter 4: Lead Selenide Nanocrystal Radiation Detectors

Properties of Nanocrystals

Colloidal quantum dots (QD) are crystalline materials with hundreds to thousands of atoms and diameter ranging from 2-20 nm [5]. These materials are often made with II-VI, III-V, and IV-VI semiconductors. Owing to their inexpensive solution based synthetic approach, tunable size-dependent band gap, small exciton binding energy, and high photoluminescence (PL) quantum yields, QDs have found applications in electronic and optoelectronic devices like solar cells, light emitting diode (LED) displays and lasers [69]. Solar cell applications are enabled by quantum confinement in QDs which give rise to charge multiplication through impact ionization. This results in QDs having high efficiency in converting incident photon energy to multiple electron-hole (e-h) pairs by enhancing carrier-carrier interactions [33]. To understand this we must consider the electronic structure of QD materials. Both bulk and NC semiconductors adhere to the band theory of the solids which describes the electronic properties [70]. In-band theory, electrons populate the valence band at 0 K, however, when an external potential is applied the electrons in the valence band gains sufficient energy to surpass the band gap and can occupy the conduction band leaving behind a hole in the valence band. Together, the electron-hole pair thus formed are called excitons [70]. Unlike bulk semiconductors, QD materials do not have a continuous valence or conduction band states. On the contrary, QD has a discrete hole and electron states which are directly dependent upon the size and geometry of the QD particles [71]. As depicted in Fig 28, the energy gaps between the highest and lowest occupied states in QD increases with decreasing size and vice versa [5].

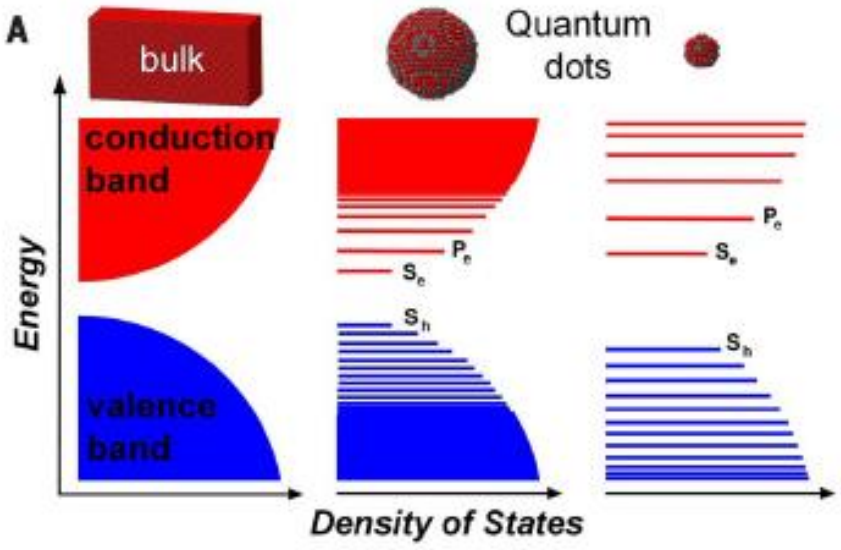

Fig 28. The electronic structure of inorganic semiconductors from bulk material to QDs of different size. Reprinted with permission from (C. R. Kagan, E. Lifshitz, E. H. Sargent, and D. V. Talapin, "Building devices from colloidal quantum dots," *Science (80-.).*, vol. 353, no. 6302, pp. 885–894, 2016). Copyright 2016 Science.

This discretization of the NC electronic states is a consequence of strong quantum confinement effect [72]. The quantum confinement effect, on the other hand, becomes prominent, when the diameter of the particle (R) is less than that of the exciton Bohr radius (a_B) [72]. Quantum confinement and its implications are discussed further in the ensuing section.

In bulk semiconductors, the creation of an exciton happens when it absorbs an individual photon of energy greater than that of its band gap (E_g) [5]. Any excess energy greater than E_g is lost in the electron-phonon interaction which leads to inefficient utilization of photon energy [73]. However, in nanocrystal semiconductors, carrier multiplication can be greatly enhanced through Impact Ionization [33]. Impact ionization is the process of formation of multiple excitons upon a single high energy photon absorption. This phenomena of multiple exciton generations (MEG) happens when the absorption of photons with energies $\geq 2E_g$ and leads to the formation of an exciton and

the subsequent relaxation to the band edge via energy transfer of at least $1E_g$ results in excitation of a second valence electron forming another exciton [73]. This is a consequence of strong dielectric and quantum confinement effects in nanoscale semiconductors where the formation of excitons with large binding energies are allowed due the to allowed transition between two discrete electronic states [5].

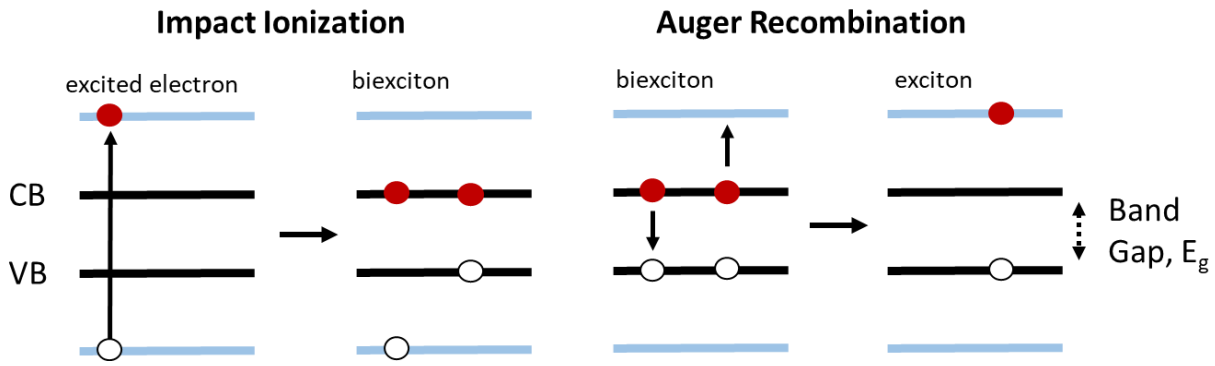

Fig 29. The schematics of II and AR processes. Reprinted with permission from (R. D. Schaller and V. I. Klimov, "High efficiency carrier multiplication in PbSe nanocrystals: Implications for solar energy conversion," *Phys. Rev. Lett.*, vol. 92, no. 18, 2004). Copyright 2004 American Physical Society.

As binding energies of the exciton and biexcitons increases with a decrease in NC size, a highly efficient non-radiative decay of multiexcitons via Auger recombination (AR) also becomes prominent [73]. This is not desirable as it counteracts the II, leading to the decay of the multiple excitons that were generated which then results in a single exciton. The AR process is more efficient in QDs compared to bulk semiconductors due to enhanced Coulomb interactions and proximal surface traps that can accommodate ejected carriers [5]. Since both II and AR are prominent in NCs, efficient methods of extracting charge carriers generated due to II, along with AR suppression is imperative to improve photon energy conversion into electric charges [33]. Ligand passivation in QD can reduce the trap density and therefore nonradiative decay of excitons can be reduced to a large extent. Also, the decay of excitons can be suppressed by growing an

epitaxial semiconductor layer on a core NC semiconductor forming a nano-heterostructure [5]. The schematics of II and Ar processes are depicted in Fig 29.

PbSe NC as a radiation detector

When compared to other semiconductors, the lead chalcogenides (PbSe, PbS, PbTe) which belong the IV-VI semiconductor group has interesting properties when used in a radiation detector. Very strong quantum confinement effects can be observed in lead chalcogenide NC with relatively large diameter resulting in MEG which is essential for higher sensitivity. This is the consequence of relatively large exciton Bohr radius for PbS, PbSe and PbTe which are 20, 46 and 50 nm respectively. Also, the relatively high density (8.3 and, 8.2 g/cm3 for PbSe and PbTe respectively) and effective atomic number (Z_{eff} = 58, 67 for PbSe and PbTe) of the lead chalcogenide materials would result in improved intrinsic efficiency for radiation detection [74]. Furthermore, Olkhovets et.al experimentally determined that the temperature coefficient of the e-h pair energies (dE/dT) decreases by more than an order of magnitude from the bulk in PbSe and PbS NCs [75]. This makes lead chalcogenide NC based radiation detectors favorable for operation at room temperature compared to bulk semiconductor-based detectors which require external cooling as is the case of bulk high purity germanium (HPGe) detectors [25]. In this thesis, we have used PbSe nanocrystals for making devices. As mentioned earlier, the strong quantum confinement in PbSe NC is possible for relatively large particle diameters. Monodisperse large diameter particles will be instrumental in improving the electronic coupling in PbSe QD films as it promotes long-range order and dense packing[76] [33]. The high density of PbSe and effective atomic number of PbSe imparts a high stopping power that is ideal for ionizing radiation detectors [77]. Also, the solution based synthesis

of PbSe QD and subsequent device fabrication can be low cost, where it could be several magnitudes less than for vacuum based single crystal radiation detectors.

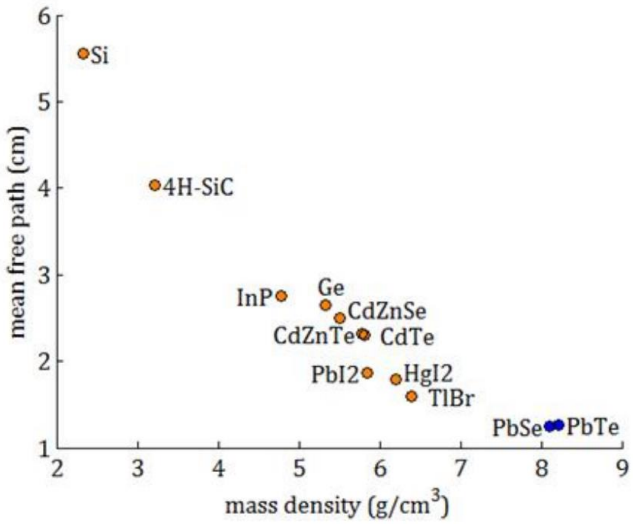

Fig 30. The mean free path for a 662 keV photon interacting with various semiconductors [78]

As in any optoelectronic devices, the success of radiation detectors based on PbSe NC depends upon the ability to form a uniform macroscopic assembly that results in a multi-stacked array of NC particles. This would allow us to generate well-defined multi-exciton states with controlled multiplicities that are highly uniform across a macroscopic NC sample following interaction with radiation [79]. Multi-excitons produced as a result of CM are independent of optical intensity, but rather the optical power ensures good resolution and detection efficiency[79]. For solution based macroscopic QD array fabrication, the shape and mono-dispersity of the NC, along with slower evaporation rate of the solvent is essential for ensuring long-range ordered NC superlattices [5]. Now the question that arises is how thick the QD films should be in order to absorb the high energy radiation. The estimation of the thickness of the radiation sensor is based on the mean free path of the incident quanta. Simulations were previously performed to estimate the mean free path of alpha, beta, gamma and X-ray in lead sulfide (PBS, a similar lead chalcogenide as PbSe) where

the values were estimated to be as ~22μm, ~200μm, ~100μm and ~10μm , respectively [25]. These values suggest a minimum thickness for the detector depending on the type of radiation. Based on Fig 30, the mean free path for a 662 keV photon interacting with PbSe would be in the range of few mm to a cm requiring a multilayer array of PbSe NC of thickness ~ 1 cm.

This estimated thickness poses many challenges in fabricating PbSe NC based radiation detectors. In conventional PbSe QD, long chain organic ligands are used as stabilizing agents during solution based synthesis. These stabilizing ligands in QD solid arrays hinders the effective charge coupling. First, they have insulating properties which result in large inter-dot potential energy barriers which impede efficient carrier transport [80]. Second, these long-chain ligand increases the inter-particle distance between the QDs further degrading the charge transport efficiency [80]. Third, these organic moieties bound to the ligand surface can absorb part of the quanta energy that should have been utilized for multiexciton generation in NC films [25]. Replacing these long chain moieties with shorter organic ligands or inorganic ligands has been proven to improve charge transport by reducing inter-particle distance and by improved electronic coupling [81]. In addition to it, alternative approaches of passivating the core NC with high band gap capping layer has also been suggested, but the creation of excitons in the bonding matrix is a drawback to this approach [25]. Different types of ligand exchange done on PbSe NC would be discussed further after the ensuing section on synthesis of nanocrystals.

Synthesis of Nanocrystals

As mentioned in an earlier section, it is of paramount importance to develop a repeatable synthetic approach to make nanocrystals or quantum dots with the desired size and shape. Non- solution based and solution-based techniques are available to create PbSe NCs [82]. Nonsolution based

synthesis approaches include molecular beam epitaxy (MBE), ion beam implantation and electron beam annealing and Stranski-Krastanov growth [82]. Solution based or wet chemistry based NC synthesis may include sol-gel, solvothermal and hydrothermal synthesis, precipitation through pH changes, precipitation by reduction, sonochemical and microwave-based synthesis [82]. Many of the non-solution based synthesis approaches require complex equipment and vacuum environment which increases complexity and cost of NC production. Also, size control in solution based synthesis is superior to that of non-solution based synthesis [25].

In this study, we have used a batch microwave synthesis approach for PbSe NC. In this method, a mixture of precursors is subject to rapid volumetric heating using a microwave [83]. This approach results in faster heating rates and smaller thermal gradients across the precursor volume. This is because the electromagnetic energy is directly converted into thermal energy inside entire volume mainly via dipolar polarization and ionic polarization mechanisms [84].

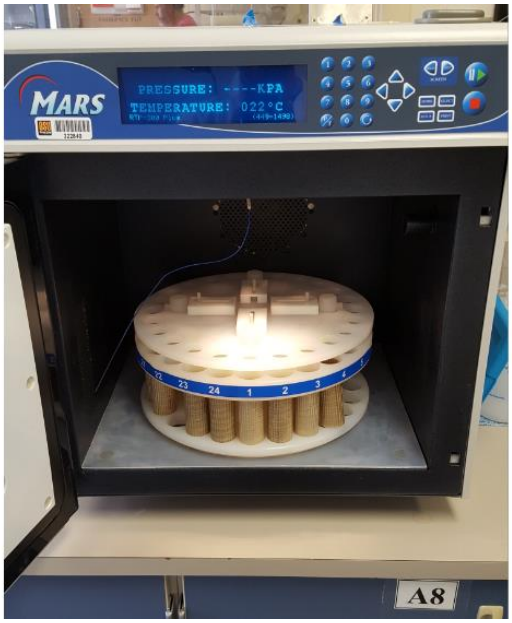

Fig 31. CEM Mars V microwave used for PbSe batch synthesis

The microwave used in this work is a CEM Mars V microwave system (Fig 31). The system can be operated with variable power output between 0 to 1800W at a maximum frequency of 2450 MHz [85]. Other major equipment used is an O_2 and H_2O free glove box and a Schlenk line.

Ligand Exchange

The strength of quantum mechanical electronic coupling between NC particles is dependent on the inter-particle distance and inter-particle matrix material [81]. The coupling energy defined by $h\Gamma$ (h, Planck's constant and Γ, the rate of carrier hopping between NC) can be improved by reducing the chain length of the stabilizing ligands and thereby enhancing the carrier hopping rate [5]. Therefore, exchanging the insulating long chain ligands with short chain ligands can improve the conductivity in a PbSe NC array. The original ligands are either replaced by shorter organic ligands or by compact inorganic ligands [71]. Ligand exchange is conducted by exposing the PbSe NC films (capped with long organic ligands) to competitive ligands which result in the exchange of the original ligands [71]. Liu et.al demonstrated the increasing in carrier mobility with alkanedithiol-treated PbSe NC [81]. This group also showed that decreasing the alkane chain length resulted in the increase in carrier mobility Amine (hydrazine and pyridine) based treatments have resulted in improvements in conductivity for PbSe NC devices [69]. Hybrid passivation treatments with thiocyanate and short chain thiols have been shown to achieve increased mobility as well as improved carrier life time by reducing inter-dot distance and by passivating surface defects [86]. The use of metal chalcogenide complexes such as SnS_4^{4-}, $Sn_2S_6^{4-}$, AsS_3^{3-}, MoS_4^{2-} were shown to have superior charge transport along with improved stability and good packing on various NC surfaces [69]. Halides (Cl^- and, I^-) and pseudo halides like SCN^- have been demonstrated to have improved charge transport on PbSe NC arrays [86].

Layer by Layer (LBL) approach of ligand exchange includes deposition of NC films via methods like spin coating, drop casting or dip coating followed by exposing the NC surface with ligand exchange solution. This cycle is continued until the desired film thickness is achieved. However, the finite penetration length of the ligand exchange solution imposes a need to limit the thickness of the NC layer deposited in one step. So in order, to deposit the required thickness would need 100s of iterations of deposition and ligand exchange which is time-consuming. This may lead to cracking and delamination of the films which is not desirable [77]. Since post-deposition ligand exchange is tedious and increases complexity, in this work we decided to do solution based ligand exchange procedures to improve conductivity.

Biphasic ligand exchange or solution based ligand exchange is an alternative approach for post-deposition ligand exchange [77]. In this approach, the hydrophobic organic ligands on NC is replaced by highly charged inorganic ligands which are accompanied by the migration of NC from apolar solvent to a polar solvent [87]. This approach has the potential to make really thick films of PbSe NC as required for a radiation detector with fewer steps as in the case of post-deposition ligand exchange. In this work, we have attempted biphasic ligand exchange of PbSe NC with methylammonium iodide (MAI) and methylammonium lead halide ($MAPbI_{3-x}\ Cl_x$) in an octane/DMF system. Biphasic ligand exchange using MAI, $MAPbI_3$, and $MAPbI_{3-x}Cl_x$ has been done earlier on PbS NC which is a similar lead chalcogenide [87][88]. However, the ligand exchange with MAI and $MAPbI_3$ in PbS (hexane/NMF) took 12-24 hours for completion [87]. In this work we will be using ligand-exchanged PbSe NCs dispersed in acetonitrile to make films.

Thus for realizing PbSe based radiation detectors, we need controlled synthesis methodologies to obtain monodisperse NC particles with desired spherical dimension, effective electronic coupling

strategies and suitable device design to capture the charge carriers when coupled with a readout circuit. This work mainly focus on developing effective ligand exchange procedure for improved packing and conductivity in PbSe NC based thin films.

Materials and Methods

Materials. Lead oxide (PbO, 99.9%) was obtained from Alfa Aesar. Selenium powder (Se, 99.9%) and trioctylphosphine (TOP, 97%), acetonitrile (99.8%) and methyl ammonium iodide (CH_3NH_3I, 99%) were acquired from Sigma Aldrich. 1-Octadecene (ODE, 90%) was purchased from TCI America. Oleic acid (OA, 90%) have been purchased from Aqua Solutions. Lead chloride ($PbCl_2$, 99%) was obtained from Acros chemicals. N, N Dimethylformamide (DMF, ACS grade) and octane (98%) were purchased from EMD Millipore and Honeywell, respectively.

PbSe NC Microwave Batch Synthesis. The recipe used for PbSe NC synthesis was developed by Eric Hostetler [82]. For the Pb precursor, a three-necked flask is charged with 1.000 g of PbO, 11.295 mL of the ODE, and 3.535 mL of OA. For the Se precursor, another three-necked flask is charged with 0.708 g of Se, 8.778 mL of the ODE, and 5.995 mL of TOP. Both of the three-necked flasks are transferred to a Schlenk line manifold and are evacuated followed by a backfill with argon. Magnetic stirrers are used to mix the individual precursors which are held for 2 hours at 150^{o}C. This ensures the complete dissolution of the Pb and Se precursors. The setup is shown in Fig 32 a. The precursors are cooled to 40^{o}C and are syringed out and are injected into two separate argon purged vials (septum sealed). The precursors are then transferred to an N_2 glove box. Inside the glovebox, 6.5 mL of Pb and Se precursors are auto pipetted into ChemGlass reaction vessels and are sealed. The reaction vessels are then placed in the CEM MARS V microwave system which then is ramped up to 140^{o}C in 4 minutes and is held for 9 minutes. The reaction vessels are

allowed to cool down to 80°C inside the microwave before taking them out and cooling them under a faucet. The reaction vessels are then transferred back into the glovebox. The color of the product post reaction can be seen in Fig 32 b.

Fig 32. a) Precursor dissolution setup w/ heating jacket. b) The reacted precursors, post-microwave step turns into a black colored solution indicating reaction completion to form PbSe NC.

PbSe NC Purification. 6 mL of the reaction product is auto pipetted into a 15 mL centrifuge tube. 2 mL of anhydrous methanol is added to the centrifuge tube to precipitate out the PbSe NC. The mixture is centrifuged for 10 minutes at 7000 rpm. The precipitated NCs attach to the walls of the centrifuge tube and supernatant can be easily decanted. The mass of the precipitated QD is measured and is re-suspended to an appropriate volume using anhydrous toluene to create PbSe NC solutions with the desired concentration.

Biphasic Ligand Exchange. 5 mL of 30 mg/mL PbSe NC in toluene is added with the equivalent amount of anhydrous ethanol to crash out the PbSe NC. The mixture is centrifuged at 5000 rpm for 5 minutes. The supernatant is decanted and the precipitated QD is re-dispersed in 5 mL of octane. 5 mL of 200mM of MAI in DMF solution or 6.5 wt % of MAI and $PbCl_2$ (molar ratio MAI: $PbCl_2$ (4:1)) mixture in DMF is added to the re-dispersed NC solution. The mixture was shaken for 2 minutes to allow the reaction to happen. The ligand exchange completion can be clearly identified by the migration of black colored QD from non-polar to polar phase. After ligand exchange, the top nonpolar solvent (octane) is syringed out and the PbSe QD solution in polar DMF solution is precipitated using anhydrous ethanol. After centrifugation, the supernatant is decanted and the PbSe NCs are re-dispersed in acetonitrile.

Field effect Transistor Fabrication PbSe QDs FETs were fabricated on a heavily p doped silicon substrate (10x15mm) with thermal oxide of thickness 100 nm. The substrate was rinsed with acetone, IPA and DI followed by blow drying with N_2 gas. The substrate was further subjected to O_2 plasma for 5 minutes. 20 μl of 100 mg/ml of ligand exchanged PbSe NC solution dispersed in acetonitrile was spun on the substrate at 1500 rpm for 30 sec. This procedure was repeated 4 times.

A Veeco thermal evaporator was used to make gold source and drain contacts (W/L = 5) with a thickness of 40 nm. The IV measurement were obtained using Agilent 4155C semiconductor parameter analyzer system in a dark room.

Radiation Detector Assembly Glass/ TO_x substrate was rinsed with acetone, IPA and DI followed by blow drying with N_2 gas. The substrate was further subjected to an O_2 plasma treatment for 5 minutes. 50 nm Ti and 200 nm Au were evaporated on the substrate. The gold surface was further subject to an O_2 plasma for 1 minute. A SU8 well with 0.8cm x 0.5 cm x 100 μm dimensions was patterned using photolithography on the substrate. For drop casting the substrate is kept on a hot plate at 50^{o}C. Now 5 μl of ligand exchanged PbSe NC solution dispersed in acetonitrile are drop cast inside the SU8 well and is allowed to dry. This is repeated for 50 times to obtain a film thickness of 7~9μm. The film is then baked at 50^{o}C for 2 hrs in a N_2 filled glove box to remove any residual solvent from the film. A 500 nm aluminum contact was thermally evaporated using Veeco thermal evaporator. The IV measurement were obtained using an Agilent 4155C semiconductor parameter analyzer in a dark room. The schematic representation of the NC radiation detector assembly and the tungsten probe positioning for IV measurements are shown in Fig 33.

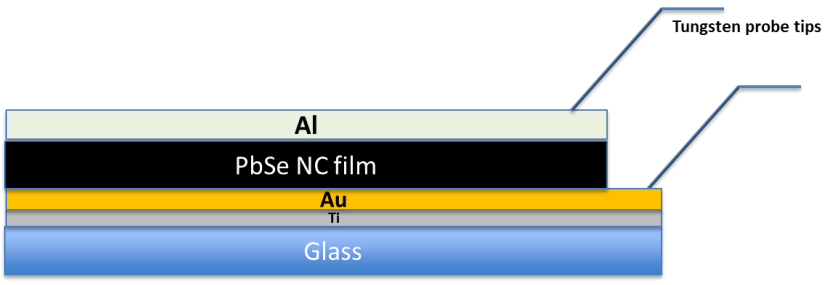

Fig 33. The schematic representation of the NC detector assembly.

Results and discussions

Fig 34 shows the absorption spectrum for oleic acid capped PbSe NC synthesized using the microwave batch method. The absorption spectra were obtained using Cary 5 UV-Vis-NIR spectrophotometer in Prof. Graham's lab at Oregon State University. We see well separated first and second excitonic peaks at 1680 nm and 1320 nm wavelength, respectively. These distinct peaks suggest that the synthesized PbSe NC obtained are monodisperse. The first excitonic peak corresponds to the intraband transition with electrons and holes having a 1S envelope function ($1S_h$-$1S_e$) [89]. The second excitonic peak corresponds to $1P_h$-$1P_e$ [89]. The noise observed on the data is due to the fact that 100 % transmission value is less than the 0% transmission, giving a negative value for the transmission ratio (T) from the sample which when converted to absorbance (abs = -log(T)) gives undefined values. We think this a minor issue with the spectrophotometer which can be ignored owing to the fact that we get a clear-cut trend of a typical PbSe NC from our synthesized particles.

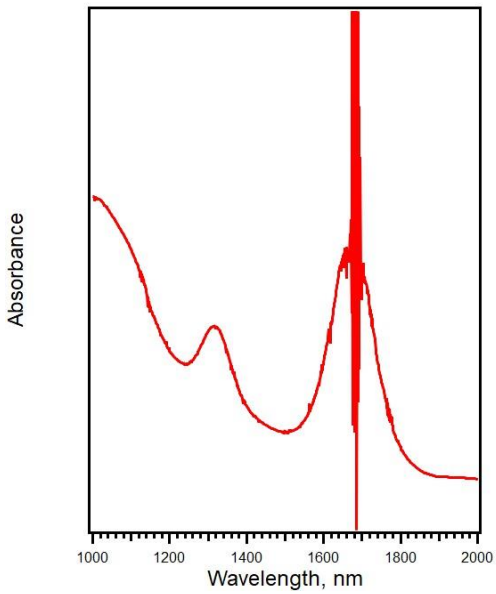

Fig 34. Absorption spectra of oleic acid capped PbSe NC in toluene.

TEM imaging of PbSe NC was done using a Titan Transmission Electron Microscope (TEM) at the CAMCOR facility at University of Oregon. These data revealed the shape and size of the typical NC particles (Fig 35 a). Crystallographic planes are visible in Fig 35 b for images obtained using HRTEM. The PbSe NCs size distribution was measured using ImageJ, and an average diameter of 6.05 ± 0.53 nm were obtained. The size distribution is shown in Fig 36.

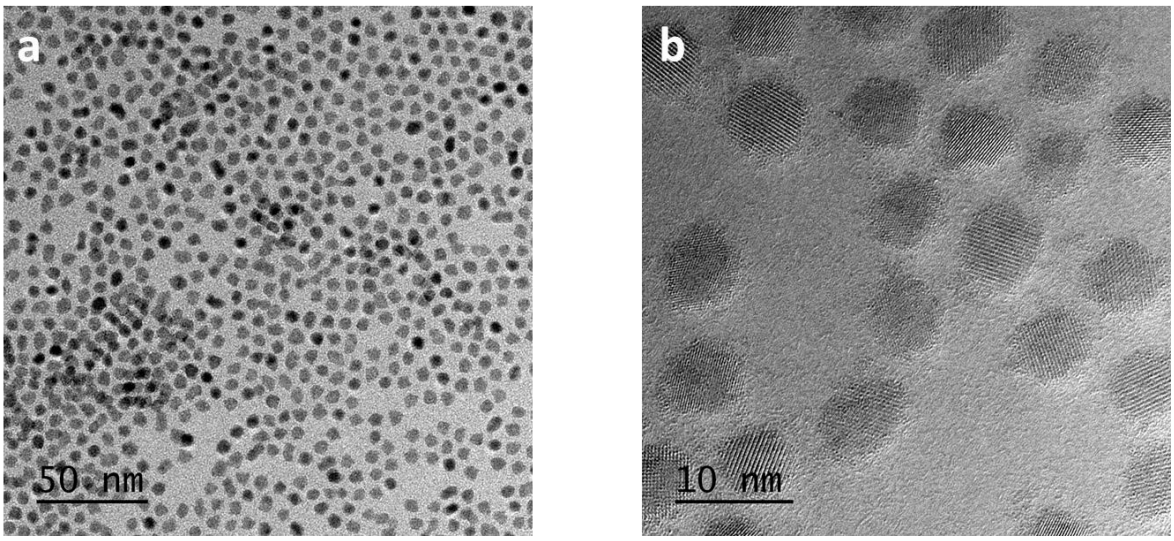

Fig 35. a) TEM Image of PbSe NC. b) HRTEM image of PbSe NC showing crystallographic planes.

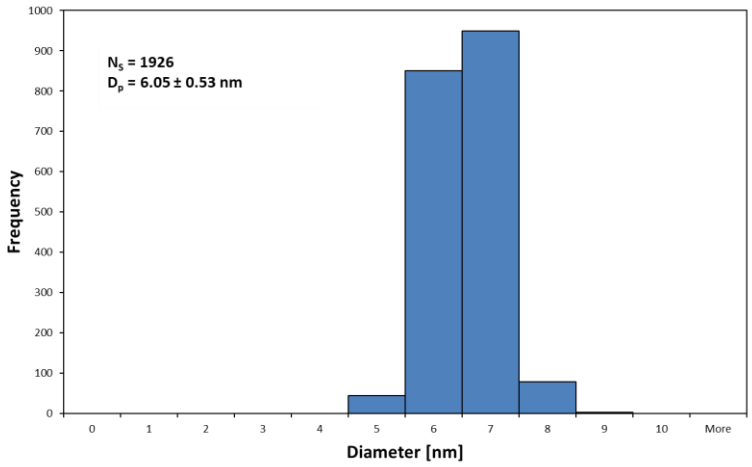

Fig 36. Particle Size Distribution of the PbSe NC– The particle size distribution created shows a particle size of 6.05 ± 0.53 nm.

Biphasic ligand exchange of the PbSe NC was done in order to improve the electronic coupling of the PbSe NC. PbSe NC dispersed in octane solution is introduced to an equivalent amount of ionic ligand solution (MAI, $MAPbI_{3-x}Cl_3$) and the mixture is shaken by hand. The completion of ligand exchange can be observed when the NC migrates to the polar solvent phase, in this case, DMF. Schematic representation of PbSe NC biphasic ligand exchange is shown in Fig 37 [77]. From Fig 38 a and 38 b we can observe the PbSe NC / Ligand exchange solution before and after ligand exchange, respectively.

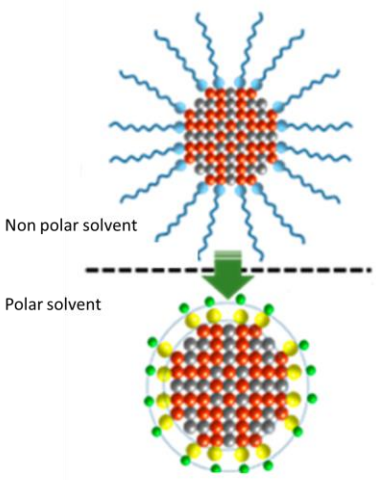

Fig 37. Schematic representation of Bi-phasic Ligand exchange procedure. Reprinted with permission from (Q. Lin *et al.*, "Phase-Transfer Ligand Exchange of Lead Chalcogenide Quantum Dots for Direct Deposition of Thick, Highly Conductive Films," *J. Am. Chem. Soc.*, vol. 139, no. 19, pp. 6644–6653, 2017). Copyright 2017 American Chemical society [77].

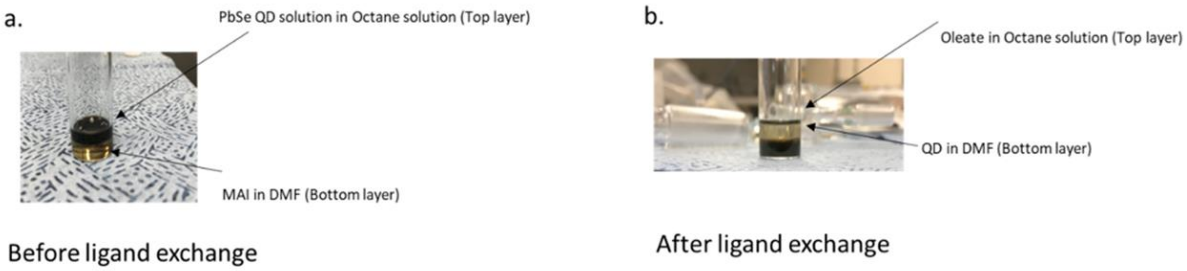

Fig 38. a) Before ligand exchange, the PbSe QD remains in the nonpolar octane solution (top layer) and, b) After ligand exchange PbSe QD transfers phase to the polar DMF phase.

The stability of the colloidal quantum dots is governed by two mechanisms: 1. steric stabilization and, 2. Electrostatic stabilization [90]. NCs with long chain hydrocarbons ligands are sterically stabilized whereas the NCs with ionic ligands are electrostatically stabilized. For a sterically stabilized NC, a good solvent is one that has a negative free energy of chain – solvent mixing such that the hydrocarbon chains repel each other and effect stabilization of the colloidal NC particles [90]. Examples include non-polar solvents like hexane, toluene, and chloroform. However, after ligand exchange, the ion passivated NC surface maintains stability only if the solvent provides dielectric screening between the oppositely charged ions [90]. Thus a solvent with a high dielectric constant like DMF, NMF, and acetonitrile can be considered a good solvent. This explains the migration of the PbSe NC particles post ligand exchange to the polar phase. The completion of the ligand exchange reaction is dependent on the affinity of the ligand to the NC surface and the relative concentration of the incoming and outgoing ligands [90].

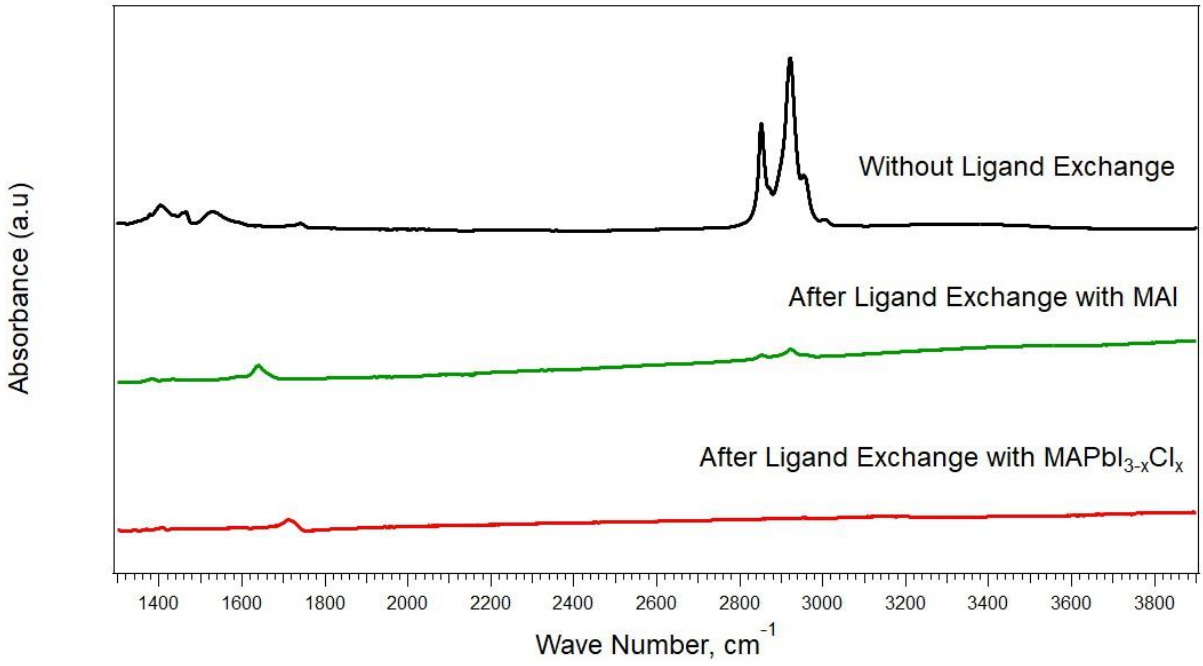

Fig 39. FTIR spectra of the drop cast film of the PbSe NC before and after ligand exchange.

Fig 39 shows FTIR spectra that were taken on the drop cast PbSe NC film to confirm the ligand exchange reaction. The signature CH stretching (2860-2920 cm^{-1}) corresponding to the long chain oleic acid is eliminated in the case of both MAI as well as $MAPbI_{3-x}Cl_x$ exchanged PbSe NC film [91].

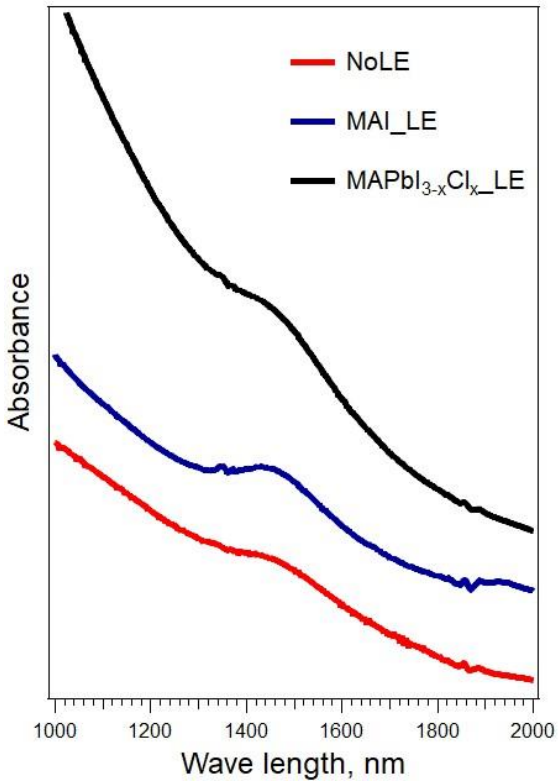

Fig 40. UV Vis NIR spectra of the drop cast film of the PbSe NC before and after ligand exchange.

UV Vis NIR absorption spectra were performed on drop cast PbSe NC films to see the effect of ligand exchange (Fig 40). When compared to the spectra obtained from the colloidal quantum dots, the intensity obtained from the PbSe films are lower. However, the presence of the first excitonic peak suggests that the quantum confinement effect is preserved in the PbSe NC films after performing ligand exchange.

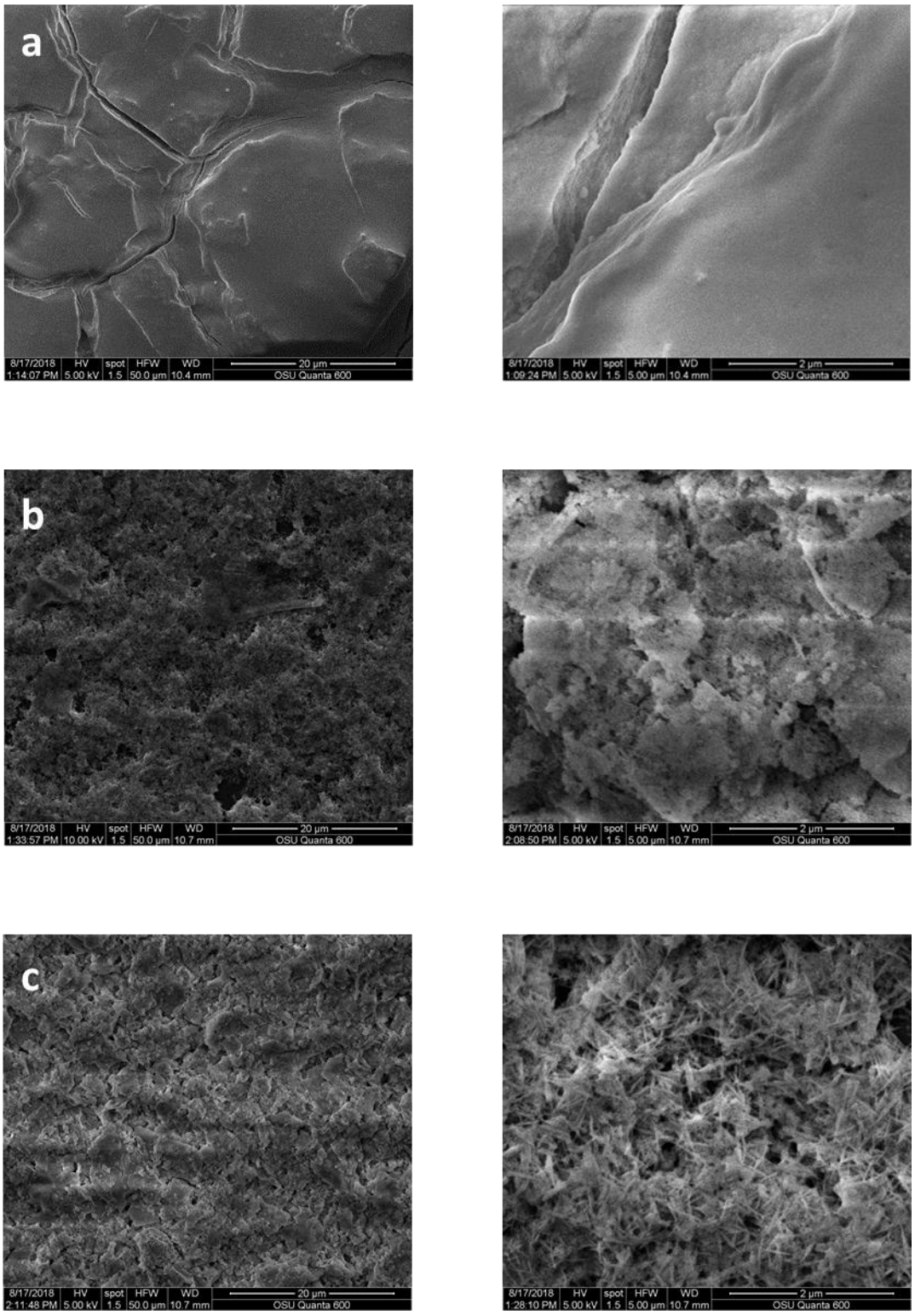

Fig 41. SEM images of drop cast PbSe NC films. a) No ligand-exchanged b) MAI ligand-exchanged c) $MAPbI_{3-x}Cl_x$ ligand-exchanged

To understand the surface morphology of the films, we obtained SEM images of the ligand-exchanged and non-ligand exchanged PbSe NC films. Fig 41 a. shows a non-ligand exchanged PbSe NC film. The surface looks shiny and smooth when compared to the ligand-exchanged ones in Fig 41 b and c. This is expected because of the presence of oily long chain stabilizing hydrocarbon ligands. Occasional ~μm cracks on the PbSe NC along with the dielectric matrix can be detrimental to the charge transport in these films. For the ligand exchanged PbSe NC films, the film morphology is rougher than the non-ligand exchanged films. Pin holes and cracks exist but the elimination of the insulating matrix is expected to increase the conductivity of the overall ligand exchanged films. $MAPbI_{3-x}Cl_x$ exchanged films shows needle like crystalline structures which can be attributed to the crystallization of the unconverted $PbCl_2$. Previously, this phenomena was observed by Cao et.al in $MAPbI_3$ perovskite films where the needle like crystalline structures of unconverted PbI_2 resulted in improved solar cell performance [92].

Surface treatment on PbSe NC	Pb atomic percentage (Pb %)	Se atomic percentage (Se %)
Nonligand exchange	65	35
MAI exchanged	61	39
$MAPbI_{3-x}$Clx exchanged	66	34

Table 3. The atomic percentage of PbSe NC after various surface treatments obtained by EDX.

Energy Dispersive X-ray Spectroscopy (EDX) was performed on these films and the results show that the atomic percentage (Pb: Se) on the non-ligand exchanged PbSe NC is 65:35 (Table 3). However, after ligand exchange with MAI, we see a decline in the atomic percentage of Pb due to the preferential etching of Pb^{2+}. However, in the case of $MAPbI_{3-x}$Clx exchanged PbSe NC the atomic percentage of Pb has increased due to the addition of Pb from $MAPbI_{3-x}Cl_x$.

Field effect measurements on ligand-exchanged PbSe NC films were done to characterize its electronic performance. The IV characteristics were obtained by measuring the drain current I_D while sweeping the gate voltage V_G from -40 V to 40 V and back down to -40V with a constant drain voltage V_D of 40 V. These measurements were conducted in air. IV curves thus obtained is shown in Fig 42.

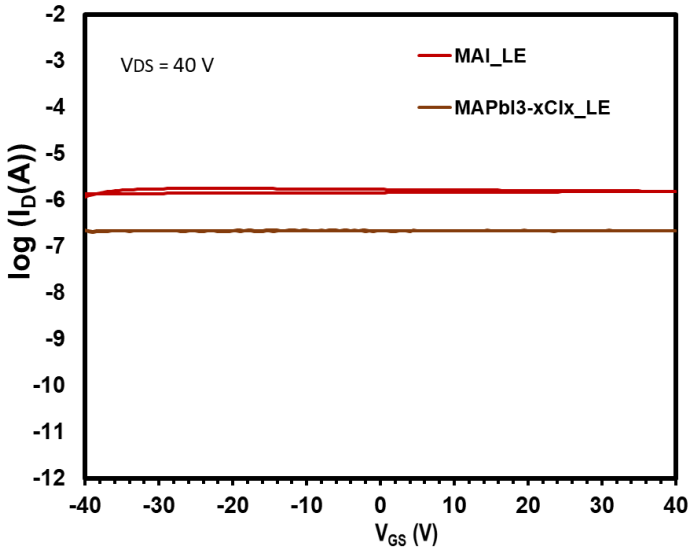

Fig 42. I-V scans of the ligand exchanged PbSe NC FET

Talapin et.al reports oleic acid capped PbSe NC FET have insulating characteristic with the highest current reaching ~pA level [93]. On treating with hydrazine it was shown that the highest current (V_D=30V, V_G= 40V) reached ~mA level which is a 9 order improvement in the conductivity of the PbSe NC film. In this work, a significant increase (~10x) in the conductivity of the films was observed after ligand-exchanged compared to non-ligand exchanged films as shown in Fig 42 [93]. In MAI and $MAPbI_{3-x}Cl_x$ ligand-exchanged films, the former showed a 6 order of magnitude

increase and while the latter showed a 5 order of magnitude increase in current. The increase in electrical conductivity is a clear measure of the improved NC packing and the reduction of the inter-particle distance between the NC particles. However, field effect characteristics were not observed in our FET measurements, which may be due to the oxidation of the PbSe NC films [94]. This is consistent with the literature, as PbSe NC films exposure to air would potentially oxidize and make them more conductive [94]. Since the NC film thickness were ~200 nm, it is expected that oxidation of the PbSe NC film would have occurred. Since the thickness of the PbSe NC films used for NC device synthesis is thicker ($\sim\mu m$) and covered with an Al top electrode, we hypothesize that the oxidation occurs at a lesser extent for the NC radiation detector devices.

Fig 43 a. shows the Gold/PbSe NC assembly whereas Fig 43 b shows the Gold/PbSe NC/Al radiation detector assembly.

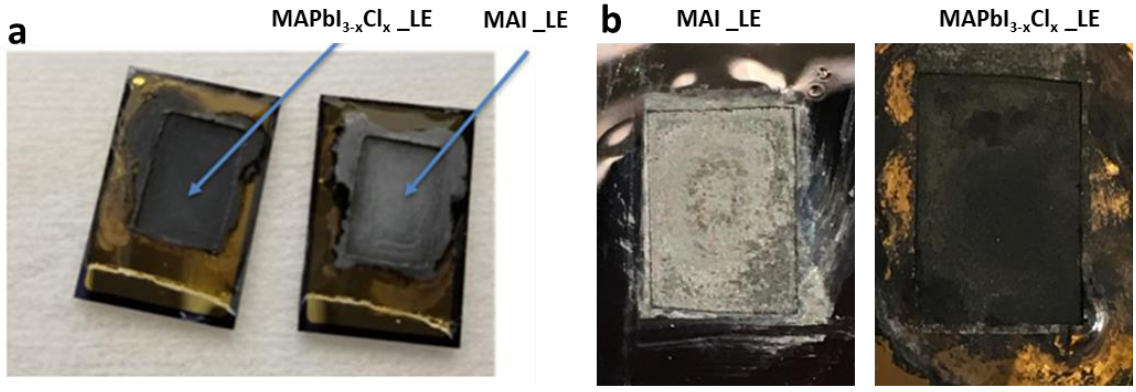

Fig 43. a) Gold/PbSe NC assembly b) Gold/PbSe NC/ Al radiation detector assembly.

The drop cast ligand-exchanged PbSe films as observed previously in SEM imaging has a very rough topography with pinholes and cracks. Therefore, we didn't get a smooth layer of aluminum on top of these films. While MAI exchanged PbSe NC films clearly shows the aluminum deposition on its surface, $MAPbI_{3-x}Cl_x$ exchanged PbSe NC films doesn't show any adhesion of aluminum particles on the surface. Previous literature suggests that this is due to the corrosion of the aluminum when in contact with hybrid perovskites which is similar to what was observed in perovskite solar cells [95]. This is corroborated by the SEM image obtained from the Helios SEM at Oregon State University. Fig 44 a. shows the Al layer on top of the MAI exchanged PbSe NC films. It shows a smooth film with occasional cracks. In Fig 44 b., we see blister like formation on the top of the perovskite exchanged films which may be due to the corrosion of Al upon reaction with perovskite [95]. However, we went ahead with the IV measurements to characterize the electrical property of the PbSe NC films.

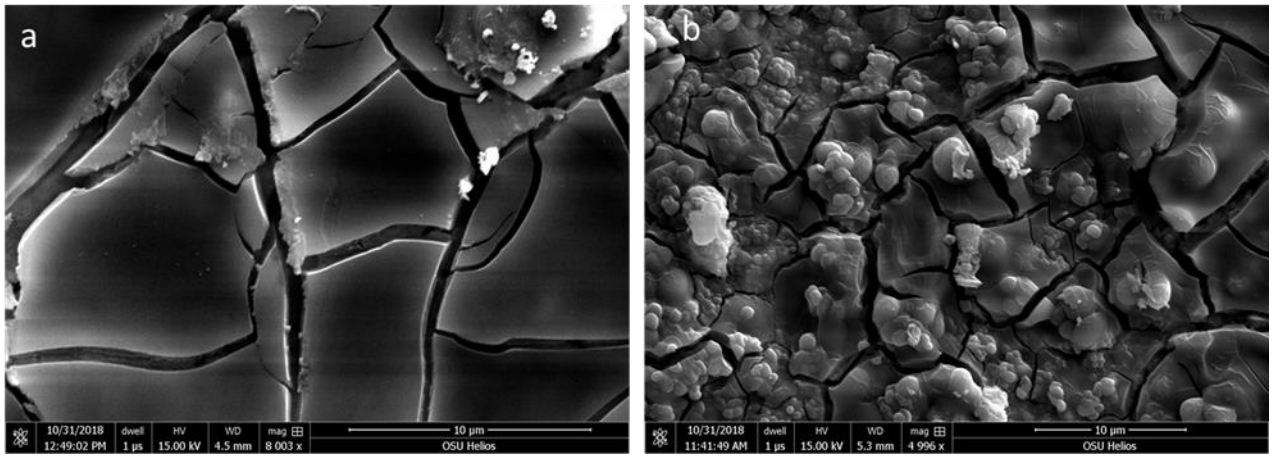

Fig 44. a) Al on MAI exchanged PbSe NC film b) Al on $MApBI_{3-x}Clx$ exchanged PbSe NC film

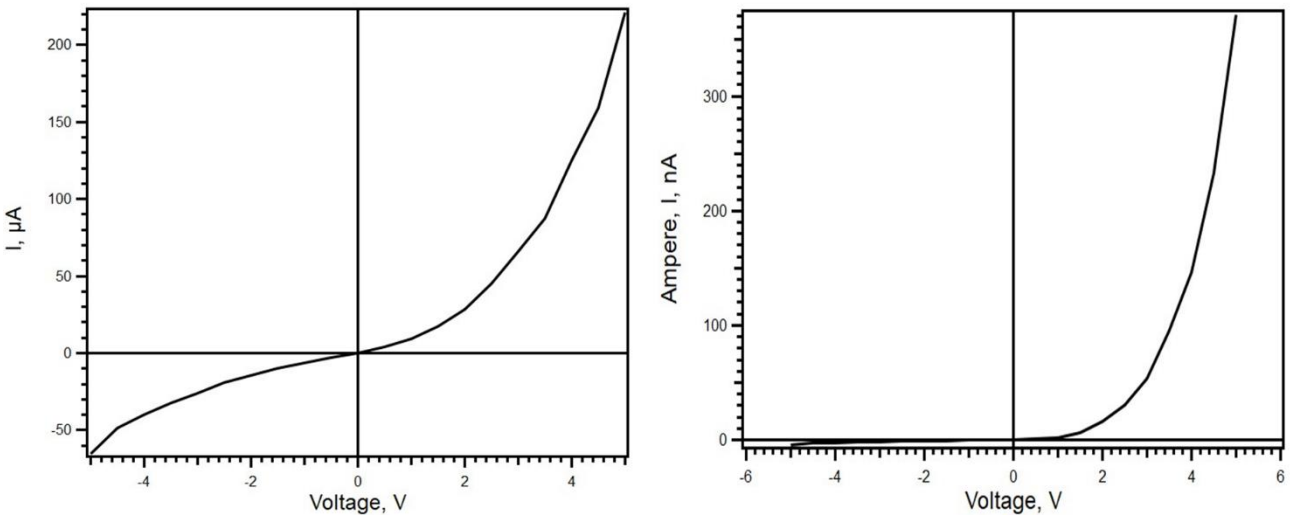

Fig 45. IV curve obtained from $MAPbI_{3-x}Clx$ exchanged PbSe NC radiation sensing assembly.

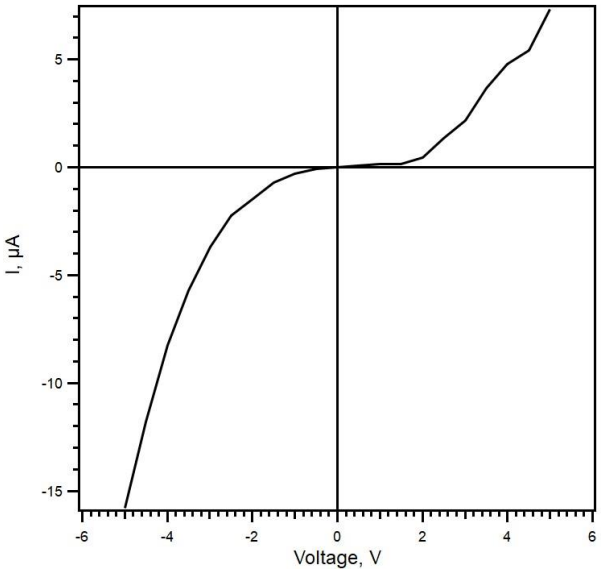

Fig 46. IV curve obtained from MAI exchanged PbSe NC radiation sensing assembly.

The IV characteristics from the radiation sensing assembly were obtained by measuring the current, I, while sweeping the voltage, V from -5 V to 5 V. Bias was applied to the Al electrode while the Au electrode was at ground. Fig 45 depicts the IV curve obtained from 2 points on the $MAPbI_{3-x}Cl_x$ exchanged radiation sensing assembly which showed Schottky like behavior. For an ideal radiation sensing assembly, the IV curve would exhibit Schottky behavior [70]. Thus these devices can be used potentially for extracting radiation sensing information. The current from the two points is of different magnitude, which may be due to the difference in thickness across the drop cast PbSe NC film or due to the poor contact made due to the corrosion of Al. For MAI exchanged PbSe NC radiation detector assembly, as shown in Fig 46, the IV curve shows Schottky behavior with current reaching a ~ μA level at 5 V. However, a large leakage current (15.8 μA at V= -5V) is observed in these devices, which is not desirable. We can attribute the non-consistent performance across the films due to the presence of cracks in Al contact and due to the non-homogeneity in the PbSe NC film. The non-homogeneity in film assembly as well as the poor metal contact strategy has to be addressed to realize reliable, high efficiency PbSe NC radiation detectors. To improve homogeneity, the optimization of the ligand exchange solution concentration is imperative to prevent the excess accumulation of ionic compounds and implementation of methanol washing at intermediate drop casting steps can be a starting point. In terms of improving the metal contact, except for copper (Cu) all other commons metals like Al, Ag and Au has been reported to have corrosive nature when in contact with perovskites [95]. Thus implementation of Cu contacts can help us achieve good metal contacts.

Chapter 5: Summary and Future Directions

Summary and Future directions for IGZO Field-Effect Sensors

In this research, we have fabricated IGZO FES capable of sensing varying concentrations of glucose in PBS solution. The range of glucose concentrations was tested, 1-20mM, mimicked the normal physiological range in interstitial fluids. The response of IGZO TFT functionalized with aminosilane demonstrated the sensitivity to varying pH values. Cross-linking GO_x to the aminosilane immobilizes the enzymes to the IGZO surface. Subsequent exposure of glucose oxidase to glucose alters the local pH at the vicinity of pH-sensitive aminosilane. This creates acceptor-like states at the IGZO interface which depletes the electron density and results in positive shift in V_{ON}. This mechanism allows IGZO FES to detect glucose with high selectivity and sensitivity. A semi-log plot of concentration versus V_{ON} indicated that a linear response could be obtained over a wide range of glucose concentrations. These results suggest that large scale integration of multiple IGZO FES into arrays could help to obtain redundant measurements of glucose and will improve the accuracy of measured glucose concentrations.

For the devices fabricated in this study, the V_{ON} in the PBS fluid was ~ 4V. From an operational standpoint, a high turn-on voltage is not desirable since it increases the sensor power consumption. The goal is to design IGZO FES as part of a portable, flexible and wearable system that integrates thin film circuits with low –voltage operation. Use of high κ dielectric like Al_2O_3, HfO_2, HfLaO, Ta_2O_5, $BaSrTiO_3$, Y_2O_3, $HoTiO_3$, $LaLuO_3$, and $LaAlO_3$ have been reported to enable low leakage current and low-voltage operation of IGZO TFTs [96]. Another alternative to reduce V_{ON} is to optimize the process recipe so as to increase the number of free charge carriers in the IGZO channel. Reduced O_2 partial pressure during deposition, and high temperature post deposition

annealing can also be employed to reduce the V_{ON} in IGZO TFT [97] [98]. However, high temperature annealing would not be a viable option for device integration on flexible substrates. Varying IGZO channel thickness is another alternative for reducing V_{ON}. Increasing the channel thickness, increases the free carrier concentration in the device, which in turn results in lower V_{ON} for IGZO TFTs [98]. Sensitivity and selectivity of the devices to a specific analyte is of paramount importance for any sensing application. While GO_x functionalization imparts selectivity to glucose, sensitivity can be improved by increasing the W/L ratio as well as by increasing the surface to volume ratio [3][13]. The effect of varying channel thickness towards the sensitivity of the IGZO FES to a specific analyte has to be investigated further. IGZO can be made completely transparent across the visible spectrum and can be integrated onto flexible substrates[44]. For such devices to be operated in visible spectrum, a sub 430 nm light filter must be integrated to overcome the sub band gap illumination based instability in IGZO[49]. The possibility of using novel patterning methods like micro- contact printing has increased the potential of integrating IGZO FES on to non –conformal surfaces to make catheters based or contact lens based devices [46]. This may open the possibility of creating a concept called Transparent Active Sensing Array (TASA), where multiple biomarker sensing capabilities can to be incorporated into a single device. However, for realizing this concept we need to further investigate more enzymes or molecules that can bind to the aminosilane base and operate in a similar mechanism as in case of glucose detection. Enzymes like lactate oxidase and uricase can be attached to the aminosilane base and their catalytic activity produces hydrogen peroxide which alter the pH at IGZO interface and can make IGZO FES selective to lactate and urea, respectively [99]. Thus, IGZO FES can be a platform for various biomarker sensing.

Summary and Future directions for PbSe NC Radiation Detectors

In this study, monodisperse PbSe NC were synthesized using a batch microwave method. PbSe NCs were confirmed using TEM imaging. The UV Vis NIR absorption spectra revealed distinct first and second excitonic peak typical for a PbSe NC. The insulating nature of PbSe NC capped with long chain hydrocarbon limits the electron transport. Therefore, we have performed ligand exchange procedures that replace the insulating ligands with shorter ionic ligands. This reduces the inter-dot distance and thereby improves conductivity of PbSe NC films. This was confirmed with field effect measurements where ligand-exchanged PbSe NC films reached current values of $\sim\mu A$. In order to overcome the limitations of post deposition ligand exchange procedure, we have integrated a biphasic ligand exchange approach into the fabrication protocol. This solution based approach has great potential for scale up to achieve thick crack free NC PbSe films. The fabricated radiation sensing assembly Al/PbSe NC/Au revealed the desirable Schottky like behaviour with moderate repeatability.

Even though it was demonstrated that the charge transport is improved, the inhomogeneity in the films has led to poor repeatability for different contact points on the PbSe NC film. This indicates that there is room for improvement in refining the fabrication protocol. Optimization of the PbSe NC solution concentration to achieve relatively thick films with minimal steps has to be investigated. The choice of metals to form a good Ohmic or Schottky contact for ligand-exchanged PbSe NC film is important for robust contact to reduce the loss of charges by phonon scattering at the contact boundary [25]. It has also been observed that after perovskite ligand-exchange metals like Al, Au, and Ag were corroded upon contact with the PbSe NC film. Therefore non- reactive metals should be used to make contacts in such cases.

PbSe NC film based on the ligand exchange treatment can be n-type or p-type [100]. $PbCl_2$ treated PbSe NC film are n-type whereas Na_2Se treated PbSe NC films are p-type [100]. This opens avenues for investigating p-n junction structure for NC radiation detector assembly with $Na_2Se/PbCl_2$ PbSe NC films. Another alternative would be to use highly doped n-type materials like ZnO or TiO_2 in a nanoparticle or sol gel with p-type PbSe NC to form p-n junction [25].

Thus by enabling thick crack free and homogeneous films, we can utilize the efficient charge multiplicity in PbSe NC to realize low cost, portable and reliable radiation sensing device capable of sensing a wide range of high energy particles.

References

[1] A. Darwish and A. E. Hassanien, “Wearable and implantable wireless sensor network solutions for healthcare monitoring,” *Sensors*, vol. 11, no. 6, pp. 5561–5595, 2011.

[2] Michael E. Porter, “How Smart, Connected Products Are Transforming Competition,” *Havard Business Review*, no. November, 2014.

[3] X. Du, Y. Li, J. R. Motley, W. F. Stickle, and G. S. Herman, “Glucose Sensing Using Functionalized Amorphous In–Ga–Zn–O Field-Effect Transistors,” *ACS Appl. Mater. Interfaces*, vol. 8, no. 12, pp. 7631–7637, 2016.

[4] Y. Yang and W. Gao, “Wearable and flexible electronics for continuous molecular monitoring,” *Chem. Soc. Rev.*, 2018.

[5] C. R. Kagan, E. Lifshitz, E. H. Sargent, and D. V. Talapin, “Building devices from colloidal quantum dots,” *Science (80-.).*, vol. 353, no. 6302, pp. 885–894, 2016.

[6] S. Hagan, E. Martin, and A. Enríquez-de-Salamanca, “Tear fluid biomarkers in ocular and systemic disease: Potential use for predictive, preventive and personalised medicine,” *EPMA J.*, vol. 7, no. 15, pp. 1–20, 2016.

[7] Kenry, J. C. Yeo, and C. T. Lim, “Emerging flexible and wearable physical sensing platforms for healthcare and biomedical applications,” *Microsystems Nanoeng.*, vol. 2, no. April, p. 16043, 2016.

[8] K. Rathee, V. Dhull, R. Dhull, and S. Singh, “Biosensors based on electrochemical lactate detection: A comprehensive review,” *Biochem. Biophys. Reports*, vol. 5, pp. 35–54, 2016.

[9] N. F. and P. E. Nikhil Bhalla, Pawan Jolly, “Introduction to Biosensors,” *Essays Biochem.*, vol. 60, pp. 1–8, 2016.

[10] X. Du *et al.*, “Fabrication of a Flexible Amperometric Glucose Sensor Using Additive Processes,” *ECS J. Solid State Sci. Technol.*, vol. 4, no. 4, pp. P3069–P3074, 2015.

[11] C. Chey, Z. Ibupoto, K. Khun, O. Nur, and M. Willander, “Indirect Determination of Mercury Ion by Inhibition of a Glucose Biosensor Based on ZnO Nanorods,” *Sensors*, vol. 12, no. 12, pp. 15063–15077, 2012.

[12] J. Kim *et al.*, “Wearable smart sensor systems integrated on soft contact lenses for wireless ocular diagnostics,” *Nat. Commun.*, vol. 8, pp. 1–8, 2017.

[13] X. Du, Y. Li, and G. S. Herman, “A field effect glucose sensor with a nanostructured amorphous In-Ga-Zn-O network,” *Nanoscale*, vol. 8, no. 43, pp. 18469–18475, 2016.

[14] M. Pumera, “Graphene in biosensing,” *Mater. Today*, vol. 14, no. 7–8, pp. 308–315, 2011.

[15] K. L. Adams, M. Puchades, and A. G. Ewing, “In Vitro Electrochemistry of Biological Systems,” vol. 1, no. 329, 2010.

[16] R. S. Chen, W. H. Huang, H. Tong, Z. L. Wang, and J. K. Cheng, “Carbon Fiber Nanoelectrodes Modified by Single-Walled Carbon Nanotubes,” *Anal. Chem.*, vol. 75, no. 22, pp. 6341–6345, 2003.

[17] H. Deng *et al.*, “Quantum dots-labeled strip biosensor for rapid and sensitive detection of microRNA based on target-recycled nonenzymatic amplification strategy,” *Biosens. Bioelectron.*, vol. 87, no. August 2016, pp. 931–940, 2017.

[18] Z. Altintas, “Applications in Biosensors and Medical Applications of Quantum Dots in Biosensors and Diagnostics,” in *Biosensors and Nanotechnology: Applications in Health Care Diagnostics*, 2018, pp. 185–199.

[19] Z. Li, Y. Wang, J. Wang, Z. Tang, J. G. Pounds, and Y. Lin, “Rapid and sensitive detection of protein biomarker using a portable fluorescence biosensor based on quantum dots and a lateral flow test strip.,” *Anal. Chem.*, vol. 82, no. 16, pp. 7008–14, 2010.

[20] H. Zhang *et al.*, “Universal Fluorescence Biosensor Platform Based on Graphene Quantum Dots and Pyrene-Functionalized Molecular Beacons for Detection of MicroRNAs,” *ACS Appl. Mater. Interfaces*, vol. 7, no. 30, pp. 16152–16156, 2015.

[21] Y.-C. Syu, W.-E. Hsu, and C.-T. Lin, “Review—Field-Effect Transistor Biosensing: Devices and Clinical Applications,” *ECS J. Solid State Sci. Technol.*, vol. 7, no. 7, pp. Q3196–Q3207, 2018.

[22] M. Kaisti, “Detection principles of biological and chemical FET sensors,” *Biosens. Bioelectron.*, vol. 98, no. June, pp. 437–448, 2017.

[23] J. R. Motley, “Application of Self-Assembled Monolayers to InGaZnO Thin Film Transistors,” Oregon State University, 2016.

[24] S. Pavlidis, “Investigation of wide band gap semiconductors: IGZO TFTs for chemical sensing and hybrid GaN / organic high-frequency packaging and circuits,” Georgia Institute of Technology August, 2016.

[25] G. Kim, “Nanocrystalline Semiconductor Nuclear Radiation Detectors,” *Univ. Michigan*, 2013.

[26] A. Kamal, *Particle Physics*. Springer, 2014.

[27] W. Binks, “Energy per ion pair.,” *Acta Radiol. Suppl.*, vol. 117, no. June, pp. 85–104, 1954.

[28] C. A. Klein, “Simple explanation of the electron-hole pair creation energy puzzle in germanium,” *Phys. Lett. A*, vol. 24, no. 10, pp. 513–514, 1967.

[29] F. Scholze, H. Rabus, and G. Ulm, “Mean energy required to produce an electron-hole pair in silicon for photons of energies between 50 and 1500 eV,” *J. Appl. Phys.*, vol. 84, no. 5, pp. 2926–2939, 1998.

[30] M. D. Hammig, “Nanoscale Methods to Enhance the Detection of Ionizing Radiation,” *Curr. Top. Ioniz. Radiat. Res.*, p. 840, 2012.

[31] S. E. Létant and T. F. Wang, “Semiconductor quantum dot scintillation under γ-ray irradiation,” *Nano Lett.*, vol. 6, no. 12, pp. 2877–2880, 2006.

[32] C. Liu, “Transparent Ultra-High-Loading Quantum Dot/Polymer Nanocomposite Monolith for Gamma Scintillation,” *ACS Nano*, vol. 11, p. 6422−6430, 2017.

[33] G. Kim, J. Huang, and M. D. Hammig, “An investigation of nanocrystalline semiconductor assemblies as a material basis for ionizing-radiation detectors,” *IEEE Trans. Nucl. Sci.*, vol. 56, no. 3, pp. 841–848, 2009.

[34] K. Y. Shin, Y. J. Tak, W.-G. Kim, S. Hong, and H. J. Kim, “Improvement of Electrical Characteristics and Stability of Amorphous Indium Gallium Zinc Oxide Thin Film Transistors Using Nitrocellulose Passivation Layer,” *ACS Appl. Mater. Interfaces*, vol. 9, no. 15, pp. 13278–13285, 2017.

[35] H. Lee, X. Zhang, J. Hwang, and J. Park, “Morphological influence of solution-processed zinc oxide films on electrical characteristics of thin-film transistors,” *Materials (Basel).*, vol. 9, no. 10, 2016.

[36] H. Pu, Q. Zhou, L. Yue, and Q. Zhang, “Solution-processed indium gallium zinc oxide thin-film transistors with infrared irradiation annealing,” *Semicond. Sci. Technol.*, vol. 28, no. 10, 2013.

[37] B. Wu and A. Kumar, “Extreme ultraviolet lithography: A review,” *J. Vac. Sci. Technol. B Microelectron. Nanom. Struct.*, vol. 25, no. 6, p. 1743, 2007.

[38] F. Zhou, B.-S. Yeh, K. A. Archila, and J. F. Wager, “Mobility Assessment of Depletion-Mode Oxide Thin-Film Transistors Using the Comprehensive Depletion-Mode Model,” *ECS J. Solid State Sci. Technol.*, vol. 3, no. 9, pp. Q3027–Q3031, 2014.

[39] A.P.P. Correia, *A Second-Order ΣΔ ADC Using Sputtered IGZO TFTs*. Springer, 2016.

[40] D. Hong, G. Yerubandi, H. Q. Chiang, M. C. Spiegelberg, and J. F. Wager, "Electrical modeling of thin-film transistors," *Crit. Rev. Solid State Mater. Sci.*, vol. 33, no. 2, pp. 101–132, 2008.

[41] R. L. Hoffman, "Zno-channel thin-film transistors: Channel mobility," *J. Appl. Phys.*, vol. 95, no. 10, pp. 5813–5819, 2004.

[42] T. Kamiya, K. Nomura, and H. Hosono, "Present status of amorphous In-Ga-Zn-O thin-film transistors," *Sci. Technol. Adv. Mater.*, vol. 11, no. 4, p. 044305, 2010.

[43] T. Kamiya, K. Nomura, and H. Hosono, "Present status of amorphous In-Ga-Zn-O thin-film transistors," *Sci. Technol. Adv. Mater.*, vol. 11, no. 4, 2010.

[44] K. Nomura, H. Ohta, A. Takagi, T. Kamiya, M. Hirano, and H. Hosono, "Room-temperature fabrication of transparent flexible thin-film transistors using amorphous oxide semiconductors," *Nature*, vol. 432, pp. 488–492, 2004.

[45] Sebastian Anthony, "IGZO display tech finally makes it to mass market: iPad Air now, high-res desktop display soon," 2013. [Online]. Available: https://www.extremetech.com/computing/170970-igzo-display-tech-finally-makes-it-to-mass-market-ipad-air-now-high-res-laptops-and-desktops-next.

[46] X. Du and G. S. Herman, "Transparent In-Ga-Zn-O field effect glucose sensors fabricated directly on highly curved substrates," *Sensors Actuators, B Chem.*, vol. 268, pp. 123–128, 2018.

[47] H. Chen, W. Jiang, L. Zhu, and Y. Yao, “Amorphous In–Ga–Zn–O powder with high gas selectivity towards wide range concentration of C2H5OH,” *Sensors (Switzerland)*, vol. 17, p. 1203, 2017.

[48] J. F. Conley, “Instabilities in amorphous oxide semiconductor Thin-Film transistors,” *IEEE Trans. Device Mater. Reliab.*, vol. 10, no. 4, pp. 460–475, 2010.

[49] S. D. Brotherton, *Introduction to thin film transistors: Physics and technology of TFTs*. 2013.

[50] X. Du, B. T. Flynn, J. R. Motley, W. F. Stickle, H. Bluhm, and G. S. Herman, “Role of Self-Assembled Monolayers on Improved Electrical Stability of Amorphous In-Ga-Zn-O Thin-Film Transistors,” *ECS J. Solid State Sci. Technol.*, vol. 3, no. 9, pp. Q3045–Q3049, 2014.

[51] T. Kamiya, K. Nomura, and H. Hosono, “Origins of High Mobility and Low Operation Voltage of Amorphous Oxide TFTs: Electronic Structure, Electron Transport, Defects and Doping*,” *J. Disp. Technol.*, vol. 5, no. 12, pp. 468–483, 2009.

[52] T. Kamiya, K. Nomura, and H. Hosono, “Electronic structures above mobility edges in crystalline and amorphous In-Ga-Zn-O: Percolation conduction examined by analytical model,” *IEEE/OSA J. Disp. Technol.*, vol. 5, no. 12, pp. 462–467, 2009.

[53] E. K.-H. Yu, S. Jun, D. H. Kim, and J. Kanicki, “Density of states of amorphous In-Ga-Zn-O from electrical and optical characterization,” *J. Appl. Phys.*, vol. 116, no. 15, p. 154505, 2014.

[54] G. T. Dang, T. Kawaharamura, M. Furuta, S. Saxena, and M. W. Allen, “Stability of In-Ga-Zn-O metal-semiconductor field-effect-transistors under bias, illumination, and temperature stress,” *Appl. Phys. Lett.*, vol. 107, no. 14, p. 143504, 2015.

[55] K. H. Ji *et al.*, “Effect of high-pressure oxygen annealing on negative bias illumination stress-induced instability of InGaZnO thin film transistors,” *Appl. Phys. Lett.*, vol. 98, no. 10, pp. 1–4, 2011.

[56] E. N. Cho, S. Member, J. H. Kang, and S. Member, “Analysis of Bias Stress Instability in Amorphous InGaZnO Thin-Film TransistorsCho, Edward Namkyu Member, Student Kang, Jung Han,” vol. 11, no. 1, pp. 112–117, 2011.

[57] M. P. Hung, D. Wang, J. Jiang, and M. Furuta, “Negative Bias and Illumination Stress Induced Electron Trapping at Back-Channel Interface of InGaZnO Thin-Film Transistor,” *ECS Solid State Lett.*, vol. 3, no. 3, pp. Q13–Q16, 2014.

[58] R. Hoffman, T. Emery, B. Yeh, and T. Koch, “21 . 4 : Zinc Indium Oxide Thin-Film Transistors for Active-Matrix Display Backplane,” *Sid*, pp. 288–291, 2009.

[59] Y. Kumaresan *et al.*, “Ultra-High Sensitivity to Low Hydrogen Gas Concentration with Pd-Decorated IGZO Film,” *IEEE Electron Device Lett.*, vol. 38, no. 12, pp. 1735–1738, 2017.

[60] H. Kim and J. Y. Kwon, “Enzyme immobilization on metal oxide semiconductors exploiting amine functionalized layer,” *RSC Adv.*, vol. 7, no. 32, pp. 19656–19661, 2017.

[61] J. M. Chalovich and E. Eisenberg, “How to Prepare Reproducible, Homogeneous, and

Hydrolytically Stable Aminosilane-derived Layers on Silica," *Langmuir*, vol. 28, no. 1, pp. 477–479, 2012.

[62] D. Kang *et al.*, "Amorphous gallium indium zinc oxide thin film transistors: Sensitive to oxygen molecules," *Appl. Phys. Lett.*, vol. 90, no. 19, pp. 10–13, 2007.

[63] J. S. Park, J. K. Jeong, H. J. Chung, Y. G. Mo, and H. D. Kim, "Electronic transport properties of amorphous indium-gallium-zinc oxide semiconductor upon exposure to water," *Appl. Phys. Lett.*, vol. 92, no. 7, pp. 90–93, 2008.

[64] F. Zhang, "Chemical Vapor Deposition of Silanes and Patterning on Silicon," Brigham Young University, 2010.

[65] Z. Ye, Y. Yuan, H. Xu, Y. Liu, J. Luo, and M. Wong, "Mechanism and Origin of Hysteresis in Oxide Thin-Film Transistor and Its Application on 3-D Nonvolatile Memory," *IEEE Trans. Electron Devices*, vol. 64, no. 2, pp. 438–446, 2017.

[66] X. He *et al.*, "Characteristics of double-gate a-IGZO TFT," *Proc. - 2014 IEEE 12th Int. Conf. Solid-State Integr. Circuit Technol. ICSICT 2014*, pp. 14–16, 2014.

[67] Y. G. Kim, Y. J. Tak, H. J. Kim, W. G. Kim, H. Yoo, and H. J. Kim, "Facile fabrication of wire-type indium gallium zinc oxide thin-film transistors applicable to ultrasensitive flexible sensors," *Sci. Rep.*, vol. 8, no. 1, pp. 1–7, 2018.

[68] S. D. Caras, D. Petelenz, and J. Janata, "pH-Based Enzyme Potentiometric Sensors. Part 2. Glucose-Sensitive Field Effect Transistor," *Anal. Chem.*, vol. 57, no. 9, pp. 1920–1923,

1985.

[69] F. Hetsch, N. Zhao, S. V. Kershaw, and A. L. Rogach, “Quantum dot field effect transistors,” *Mater. Today*, vol. 16, no. 9, pp. 312–325, 2013.

[70] D. W. Rinaldi, “Radiation Detection using a Semiconducting Nanocrystal Detector,” Oregon State University, 2016.

[71] D. V. Talapin, J.-S. Lee, M. V. Kovalenko, and E. V. Shevchenko, “Prospects of Colloidal Nanocrystals for Electronic and Optoelectronic Applications,” *Chem. Rev.*, vol. 110, no. 1, pp. 389–458, 2010.

[72] Jeffrey Matthew Harbold, “The electronic and optical properties of colloidal lead- selenide semiconductor nanocrystals,” Cornell University, 2005.

[73] R. D. Schaller and V. I. Klimov, “High efficiency carrier multiplication in PbSe nanocrystals: Implications for solar energy conversion,” *Phys. Rev. Lett.*, vol. 92, no. 18, pp. 1–4, 2004.

[74] G. Kim and M. D. Hammig, “An investigation of single-crystal PbTe for nuclear radiation detector applications,” in *IEEE Nuclear Science Symposium Conference Record*, 2011, pp. 1732–1737.

[75] A. Olkhovets, R. C. Hsu, A. Lipovskii, and F. W. Wise, “Size-dependent temperature variation of the energy gap in lead-salt quantum dots,” *Phys. Rev. Lett.*, vol. 81, no. 16, pp. 3539–3542, 1998.

[76] F. Remacle, K. C. Beverly, J. R. Heath, and R. D. Levine, “Conductivity of 2-D Ag quantum dot arrays: Computational study of the role of size and packing disorder at low temperatures,” *J. Phys. Chem. B*, vol. 106, no. 16, pp. 4116–4126, 2002.

[77] Q. Lin *et al.*, “Phase-Transfer Ligand Exchange of Lead Chalcogenide Quantum Dots for Direct Deposition of Thick, Highly Conductive Films,” *J. Am. Chem. Soc.*, vol. 139, no. 19, pp. 6644–6653, 2017.

[78] M. D. Hammig, “Silicon-Based Examination of Gamma-Ray and Neutron Interactions,” University of Michigan, 2018.

[79] R. D. Schaller and V. I. Klimov, “Non-poissonian exciton populations in semiconductor Nanocrystals via carrier multiplication,” *Phys. Rev. Lett.*, vol. 96, no. 9, pp. 1–4, 2006.

[80] C. H. Jo *et al.*, “Low-temperature annealed PbS quantum dot films for scalable and flexible ambipolar thin-film-transistors and circuits,” *J. Mater. Chem. C*, vol. 2, no. 48, pp. 10305–10311, 2014.

[81] Y. Liu *et al.*, “Dependence of carrier mobility on nanocrystal size and ligand length in pbse nanocrystal solids,” *Nano Lett.*, vol. 10, no. 5, pp. 1960–1969, 2010.

[82] E. B. Hostetler, “Processing of Nanoscale Materials,” Oregon State University, 2013.

[83] M. A. Sliem, A. Chemseddine, U. Bloeck, and R. A. Fischer, “PbSe nanocrystal shape development: Oriented attachment at mild conditions and microwave assisted growth of nanocubes,” *CrystEngComm*, vol. 13, no. 2, pp. 483–488, 2011.

[84] M. B. Schütz, L. Xiao, T. Lehnen, T. Fischer, and S. Mathur, "Microwave-assisted synthesis of nanocrystalline binary and ternary metal oxides," *Int. Mater. Rev.*, vol. 63, no. 6, pp. 341–374, 2018.

[85] CEM corporation, "Operation manual CEM MARS," 2016.

[86] S. J. Oh *et al.*, "Engineering the surface chemistry of lead chalcogenide nanocrystal solids to enhance carrier mobility and lifetime in optoelectronic devices," *Chem. Commun.*, vol. 53, no. 4, pp. 728–731, 2017.

[87] D. M. Balazs *et al.*, "Colloidal Quantum Dot Inks for Single-Step-Fabricated Field-Effect Transistors: The Importance of Postdeposition Ligand Removal," *ACS Appl. Mater. Interfaces*, vol. 10, no. 6, pp. 5626–5632, 2018.

[88] M. Sytnyk *et al.*, "Quasi-epitaxial Metal-Halide Perovskite Ligand Shells on PbS Nanocrystals," *ACS Nano*, vol. 11, no. 2, pp. 1246–1256, 2017.

[89] M. T. Trinh, A. J. Houtepen, J. M. Schins, J. Piris, and L. D. A. Siebbeles, "Nature of the second optical transition in PbSe nanocrystals," *Nano Lett.*, vol. 8, no. 7, pp. 2112–2117, 2008.

[90] M. A. Boles, D. Ling, T. Hyeon, and D. V. Talapin, "Erratum: The surface science of nanocrystals (Nature Materials (2016) 15 (141-153))," *Nat. Mater.*, vol. 15, no. 3, p. 364, 2016.

[91] M. H. Zarghami, Y. Liu, M. Gibbs, E. Gebremichael, C. Webster, and M. Law, "p-Type

PbSe and PbS Quantum Dot," *ACS Nano*, vol. 4, no. 4, pp. 2475–2485, 2010.

[92] D. H. Cao *et al.*, "Remnant PbI2, an unforeseen necessity in high-efficiency hybrid perovskite-based solar cells?," *APL Mater.*, vol. 2, no. 9, pp. 1–8, 2014.

[93] D. V Talapin and C. B. Murray, "PbSe Nanocrystal Solids for n-and p-Channel Thin Film Field-Effect Transistors," *Science (80-.).*, vol. 310, no. 86, pp. 86–90, 2005.

[94] J. M. Luther, M. Law, Q. Song, C. L. Perkins, M. C. Beard, and A. J. Nozik, "Structural, optical, and electrical properties of self-assembled films of PbSe nanocrystals treated with 1,2-ethanedithiol," *ACS Nano*, vol. 2, no. 2, pp. 271–280, 2008.

[95] J. Zhao *et al.*, "Is Cu a stable electrode material in hybrid perovskite solar cells for a 30-year lifetime?," *Energy Environ. Sci.*, vol. 9, no. 12, pp. 3650–3656, 2016.

[96] P. Ma *et al.*, "Low voltage operation of IGZO thin film transistors enabled by ultrathin Al2O3gate dielectric," *Appl. Phys. Lett.*, vol. 112, no. 2, pp. 1–5, 2018.

[97] E. Chong, Y. S. Chun, S. H. Kim, and S. Y. Lee, "Effect of oxygen on the threshold voltage of a-IGZO TFT," *J. Electr. Eng. Technol.*, vol. 6, no. 4, pp. 539–542, 2011.

[98] W. P. Zhang, S. Chen, S. B. Qian, and S. J. Ding, "Effects of thermal annealing on the electrical characteristics of In-Ga-Zn-O thin-film transistors with Al2O3gate dielectric," *Semicond. Sci. Technol.*, vol. 30, no. 1, 2015.

[99] Matsumoto, "Sensor storage solution, sensor calibration solution and sensor," US 2004/0185568A1, 2004.

[100] S. J. Oh *et al.*, “Designing high-performance PbS and PbSe nanocrystal electronic devices through stepwise, post-synthesis, colloidal atomic layer deposition,” *Nano Lett.*, vol. 14, no. 3, pp. 1559–1566, 2014.